2013

The development of an AC magneto- optic Kerr effect system for the characterization of pulsed laser deposited Co_2MnSi-xAl1-x Heusler alloy thin films

Matthew Stephen Champagne
Louisiana State University and Agricultural and Mechanical College, mchamp9@tigers.lsu.edu

THE DEVELOPMENT OF AN AC MAGNETO-OPTIC KERR EFFECT SYSTEM FOR THE CHARACTERIZATION OF PULSED LASER DEPOSITED $Co_2MnSi_xAl_{1-x}$ HEUSLER ALLOY THIN FILMS

A Thesis

Submitted to the Graduate Faculty of the
Louisiana State University and
Agricultural and Mechanical College
in partial fulfillment of the
requirement for the degree of
Master of Science

in

The Department of Physics and Astronomy

by
Matthew Champagne
B.S, Louisiana State University and Agricultural and Mechanical College, 2010
May 2013

Acknowledgements

I owe a great deal of gratitude to Dr. Shane Stadler, my advisor, who has helped through every step of this thesis. His patience, understanding, guidance and knowledge have allowed me to put together this thesis is such a short period of time. I must also acknowledge Joe Prestigiacomo for the introduction into the laboratory and invaluable help in learning many of the important aspects of the PLD system and the lab. It is also necessary to thank Ahmad Saleheen and Nathan Glueck, as fellow students of the lab, who helped to learn the new processes, setup the equipment, and run the experiments.

I would like to thank Dr. Shane Stadler, Dr. David Young, and Dr. Daniel Sheehy, my committee members, for their patience and comments during my thesis defense.

I would like to thank the Department of Physics and Astronomy, for the teaching assistantship for two years, and Dr. Shane Stadler for the research assistantship while I worked on this thesis.

Finally, I must thank my family and friends who have supported me through school. Their understanding, patience, and support have helped motivate and push me through such a difficult process.

Table of Contents

List of Tables

List of Figures

Abstract

The Kerr rotation and Kerr ellipticity of thin films can be measured using an AC magneto-optic Kerr effect (AC-MOKE) system. The longitudinal MOKE measurements were taken for a series of $Co_2MnSi_xAl_{1-x}$ thin films with values of x= 0.00, 0.25, 0.50, 0.75, 1.00. The films were fabricated using ultra high vacuum, pulsed laser deposition (PLD) techniques. The PLD targets were made using conventional arc-melting techniques. Using a Jones matrix analysis, it was shown that the Kerr rotation and Kerr ellipticity can be measured separately using two optical setups by taking advantage of a photoelastic modulator and lock-in techniques.

Co_2MnAl and Co_2MnSi are both in a class of materials known as Heusler alloys and are predicted to have a high degree of spin polarization. The crystal structure was confirmed as the $L2_1$ using powder x-ray diffraction. The lattice constants were shown to be 5.61Å and 5.77 Å for Co_2MnSi andCo_2MnAl, respectively. For each film, the DC-MOKE, AC-Kerr rotation, and AC-Kerr ellipticity were measured. The DC-MOKE loops were used to estimate the total Kerr rotation. There was no noticeable trend in the values of the total Kerr rotation as calculated using a technique based on Malus' law. The Kerr rotation showed a decreasing trend with concentration (x). The sample with x=0.50 was calculated to be the same as the one with x=0.00 value. The Kerr ellipticity also decreased as x was increased. There have been no reports in the literature on direct measurements of the Kerr rotation or ellipticity for $Co_2MnSi_xAl_{1-x}$ for any values of x. The measurements gave values that were comparable to reported calculations and measured values of similar Heusler alloys.

Chapter 1
Magneto-Optic Effects

1.1 History and Introduction

In 1845 Michael Faraday published his initial observation of the change in polarization of light as it passed through a transparent material that was subjected to a magnetic field. Faraday's experiment, although simple to setup by modern standards, produced profound results. He used an oil lamp as a light source, which was polarized by reflection from a glass surface. The polarized ray was then passed through a transparent material placed between the poles of a powerful electromagnet. The power of the magnetic field was not given in terms of modern units, but was said to be able to "sustain a weight of twenty-eight to fifty-six, or more, pounds." [1] The beam was finally analyzed by a revolving Nicholas' eyepiece, an optic used to polarize light. After several failed attempts using various transparent materials such as air and water, Faraday used heavy glass (silicate borate of lead) as the transparent material. This produced a noticeable rotation in the polarization of the transmitted ray. Although the measurements were taken by sight, Faraday was able to determine that various materials would induce different rotations, i.e., turpentine produced roughly twice the rotation of the heavy glass, etc. [1]. This rotation phenomenon became known as the Faraday Effect.

Approximately thirty years later, John J. Kerr discovered a similar effect upon *reflection* rather than transmission of the beam. The optics used were only slightly more sophisticated. Using a paraffin-flame as a light source, Kerr created a polariscope with two Nicol prisms. A Nicol prism is an optic that takes advantage of the birefringence of the material to internally reflect one polarized ray while transmitting the complementary polarized component. The light passed through the first Nicol prism, linearly polarizing the ray which was then reflected from

the pole of a highly polished horseshoe electromagnet with an angle of incidence between 60 and 80 degrees as measured from the normal. The reflected beam was then passed through another Nicol prism, which was rotated so that the transmission axis was perpendicular with respect to the first prism. In the absence of an applied magnetic field, the polariscope produced an extinction condition in which no light was transmitted. After turning on the magnet, the polarization was immediately changed, producing a small amount of light transmitted through the analyzing Nicol prism [2].

Kerr then took the experiment farther by rotating the analyzer through a small angle, allowing a small amount of light to pass through it. He observed that the intensity of the transmitted light was dependent upon the polarity of the magnet. Kerr concluded that reversing the direction of the magnetic field reversed the rotation of the polarization. In Kerr's own words: "A true south pole of polished iron, acting as a reflector, turns the polarization righhandedly." [2] If the poles were reversed, the rotation would be a left-handed rotation. Using the fact that compression and tension on a glass slide would rotate the polarization of the ray, Kerr was able to confirm the right-handed and left-handed change in rotation. He ran into some experimental difficulty since the compression and tension were done by hand. Also, contamination of the surface (including by his breath) required the replacement of the slide [2]. Although the reflected phenomenon is similar to the Faraday Effect, it became known as the magneto-optic Kerr effect (MOKE).

Since Kerr's discovery, there were several attempts to accurately describe the phenomenon. Argyres was the first to accurately describe it in 1955 where he concluded that the coupling between the electric field vector and the spin of the electron interacting via the spin-

orbit interaction is the source of the magneto-optic effect [3, 4]. Argyres showed this quite rigorously, but the details are beyond the scope of this thesis.

Not until the mid-1980's did MOKE techniques gain popularity among experimentalists. It was Mooge and Bader who demonstrated the sensitivity (and therefore usefulness) of MOKE measurements. In 1985 they measured magnetic hysteresis loops of epitaxial iron monolayer films grown on Au (100) [5]. They also coined the term "surface magneto-optic Kerr effect" (SMOKE) to refer to MOKE when applied to ultrathin films and surfaces. In 1991 Lui and Bader wrote "Issues in Surface Magnetism" to illustrate the applications and science that could be addressed with the use of MOKE, which brought a broad interest to the technique [6,7]. Since then it has become a standard method for measuring the magnetic properties of films.

1.2 Theory

Before going into great detail about the mechanism behind MOKE, it is helpful to briefly outline how linear polarized light obtains a rotation and ellipticity. Linearly polarized light can be represented as a superposition of right circularly polarized light (RCP) and left circularly polarized light (LCP) in equal parts, with both components in phase. The index of refraction, *n*, can be expressed as a complex quantity,

$$n = n_r + in_i\,, \tag{1.1}$$

where n_r is the real and n_i the imaginary component of the complex index. If there is a difference in n_r between RCP and LCP light in a given material, there will be a phase shift in the transmitted (or reflected) beam due to the differences of the speed of light in the medium. This phase shift will result in a rotation of the original polarization. A difference in n_i for RCP and

LCP light will cause a difference in the absorption rates of these components. This will produce a difference in the amplitude of RCP and LCP light, and result in a change in the ellipticity (the ratio between the major and minor axis) [4].

Argyres first described in great detail the mechanism behind MOKE in 1955 [3]. Since the early 1990's it has been presented in several ways, making it more accessible to those interested in the use of MOKE to find the total Kerr rotation[4, 8]. Before defining the Kerr rotation and Kerr ellipticity, it is important to discuss the differences in polarized light since it plays a crucial role in measurements. Linear polarization of light is defined by the direction of the electric field of the light in reference to the plane of incidence. The case where the electric field vector is parallel to the plane of incidence is referred to as p-polarization. With s-polarized light, the electric field vector is perpendicular to the plane of incidence. (See Figure 1.1)

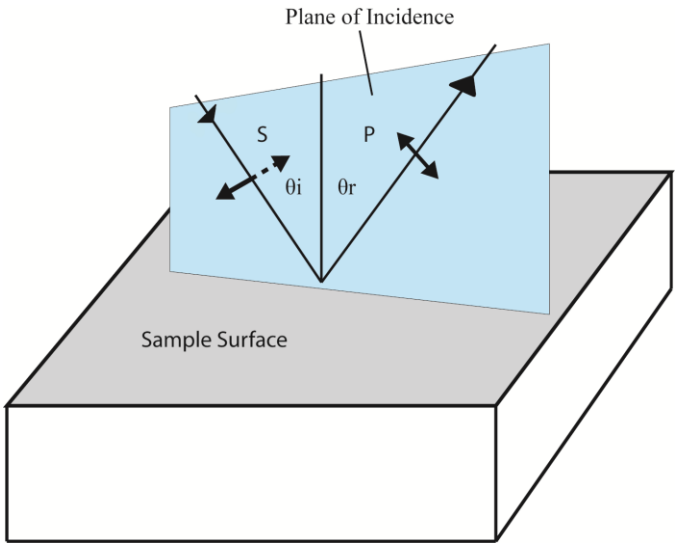

Figure 1.1 The plane of incidence is the plane that is defined by the incident and reflected beam. S-polarized light is perpendicular to the plane of incidence while p-polarized light is parallel to the plane of incidence.

Although the incident beam may be perfectly s- or p-polarized, the reflected beam will generally have both s- and p- components due to an induced rotation and ellipticity. The *total*

(effective) Kerr rotation, φ_i, is the combined effect of the Kerr rotation and the change in ellipticity, where *i* represents either s- or p- polarized light. The relationship between the reflected light and the **total Kerr rotation** (given separately for s- and p- polarization) is given by:

$$\varphi_p = \varphi_p' + i\varphi_p'' = \frac{r_{sp}}{r_{pp}} \tag{1.2}$$

$$\varphi_s = \varphi_s' + i\varphi_s'' = \frac{r_{ps}}{r_{ss}}, \tag{1.3}$$

where φ_i' is the Kerr rotation, φ_i'' is the Kerr ellipticity, and r_{ij} is the ratio of the reflected j-polarized electric field divided by the incident i-polarized electric field. The total Kerr rotation is the effective rotation that takes into account the Kerr rotation and Kerr ellipticity. In general the equations for the reflection coefficients are quite complex, but they can be simplified somewhat by assuming that the total optical thickness, *nd*, of the film is much less than wavelength of the light

$$\sum_i n_i d_i \ll \lambda, \tag{1.4}$$

where n_i is the index of refraction for the *i*th layer, and d_i is the thickness of the layer. This assumption, which allows for the use of the simplified reflection coefficients, is also the distinction between MOKE and SMOKE. If the optical thickness of the measured film is much greater than the wavelength, the bulk properties will dominate, and the surface effects will not be as prevalent.

To begin the discussion of the theory one must examine the generalized 3x3 dielectric tensor:

$$\tilde{\varepsilon} = \begin{pmatrix} \varepsilon_{xx} & \varepsilon_{xy} & \varepsilon_{xz} \\ \varepsilon_{yx} & \varepsilon_{yy} & \varepsilon_{yz} \\ \varepsilon_{zx} & \varepsilon_{zy} & \varepsilon_{zz} \end{pmatrix} . \tag{1.5}$$

In a magnetic sample, off-diagonal terms are generally antisymetric, (i.e. $\varepsilon_{xy} = -\varepsilon_{yx}$) and can be used to reduce the tensor to a more usable form given by

$$\tilde{\varepsilon} = \varepsilon_{xx} \begin{pmatrix} 1 & -iQm_z & iQm_y \\ iQm_z & 1 & iQm_x \\ -iQm_y & iQm_x & 1 \end{pmatrix} , \tag{1.6}$$

where Q is the magneto-optic constant given by $Q = i\,\varepsilon_{xy}/\varepsilon_{xx}$. For simplicity we assume $\varepsilon_{xx} = \varepsilon_{yy} = \varepsilon_{zz}$, meaning the sample is treated as isotropic when not in an applied magnetic field. We can also assume that the off-diagonal terms have the same magnitude [13]. This is justified since only one value is measured at a time due to the geometry of the experimental setup (this will be discussed in greater detail later). Finally, $m_x, m_y,$ and m_z are defined as the directional cosines of the magnetization vector:

$$\begin{aligned} m_x &= \sin\varphi \cos\gamma \\ m_y &= \sin\varphi \sin\gamma \\ m_z &= \cos\varphi \end{aligned} \tag{1.7}$$

where φ and γ are defined in Figure 1.2. Solving the above tensor for the eigenvalues will lead to two normal modes of the dielectric, which correspond to RCP and LCP. If the tensor is symmetric (i.e., $Q = 0$), this will lead to a dielectric constant rather than the two normal modes.

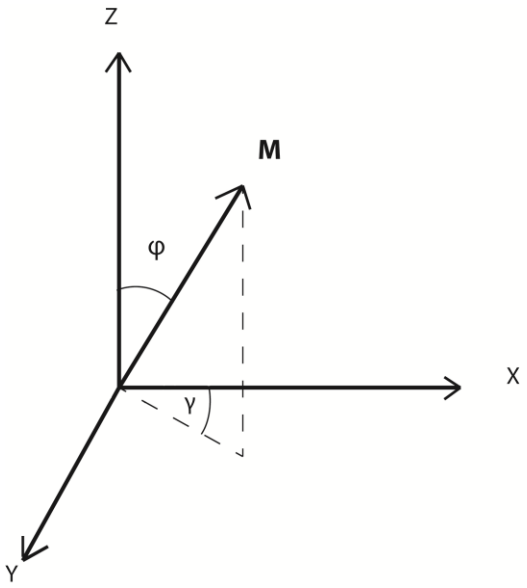

Figure 1.2. The angle φ is defined as the angle between the magnetization vector and the z-axis while γ is the angle between the projection of the magnetization vector in the xy-plane and the x axis.

Although the two modes essentially show that RCP and LCP light have two different indices of refraction, it is not useful for calculating the rotation of the polarization of the reflected light. For such calculations, one must determine the magneto-optic Fresnel reflection matrix:

$$\hat{R} = \begin{pmatrix} r_{pp} & r_{ps} \\ r_{sp} & r_{ss} \end{pmatrix}, \tag{1.8}$$

where the components of the matrix have been defined in Equation (A.7).

To find the components of the reflection matrix (Equation (1.8)) one must define a medium boundary matrix A_j for the j^{th} layer and a propagation matrix D_j for the j^{th} layer (for detailed definitions see appendix A). A_j characterizes the electric field as the light passes from one medium to the next. D_j describes the propagation of the light through the magnetic medium. These are used to find a matrix, M, that relates the incident, reflected, and transmitted electric field amplitudes:

$$M = {A_0}^{-1} A_1 D_1 {A_1}^{-1} A_2 \, . \tag{1.9}$$

The resultant 4x4 matrix can be represented as a set of 2x2 block matrices [9-12]

$$M = \begin{pmatrix} G & H \\ I & J \end{pmatrix}. \tag{1.10}$$

Although these can be used to relate the transmitted and reflected amplitudes, the reflected amplitudes are all that are needed for Kerr measurements. The elements of *M* are related to the Fresnel reflection coefficients by

$$\begin{pmatrix} r_{pp} & r_{ps} \\ r_{sp} & r_{ss} \end{pmatrix} = IG^{-1}. \tag{1.11}$$

The simplified Fresnel coefficients r_{ss} and r_{pp} are given by [11, 12]

$$r_{ss} = \frac{n_0 \cos\theta_0 - n_s \cos\theta_2}{n_0 \cos\theta_0 + n_s \cos\theta_2} + \frac{4\pi i n_0 d \cos\theta_0 ({n_1}^2 cos^2\theta_1 - {n_s}^2 cos^2\theta_2)}{\lambda (n_0 \cos\theta_0 + n_s \cos\theta_2)^2} \tag{1.12}$$

and

$$r_{pp} = \frac{n_s \cos\theta_0 - n_0 \cos\theta_2}{n_s \cos\theta_0 + n_0 \cos\theta_2} + \frac{4\pi i n_0 d \cos\theta_0 ({n_s}^2 cos^2\theta_1 - {n_1}^2 cos^2\theta_2)}{\lambda (n_0 \cos\theta_0 + n_s \cos\theta_2)^2}, \tag{1.13}$$

where $n_0, n_1,$ and n_s are the indices of refraction for the first medium, the second medium, and the substrate, respectively, while $\theta_0, \theta_1,$ and θ_2 are the angles of the electric field with respect to the normal (see Figure 1.3).

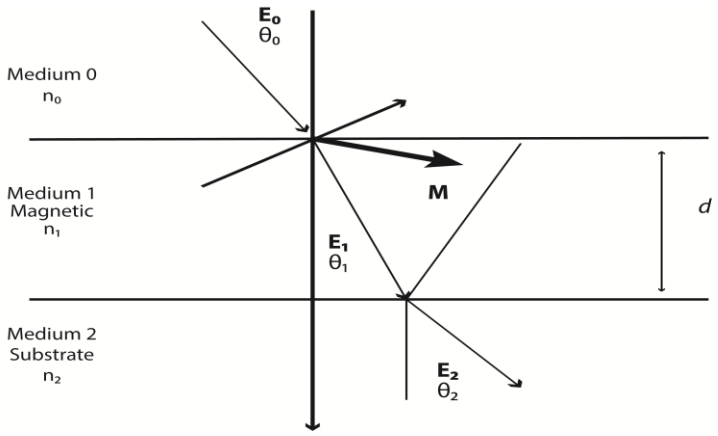

Figure 1.3 The incoming electric field will be bent as it enters the next medium according to Snell's law [12].

1.3 SMOKE

To discuss the off-diagonal terms of the reflection matrix it is necessary to understand the different possible configurations of MOKE. There are three alignments of the applied magnetic field with respect to the sample and the plane of incidence that are of importance. The first is polar MOKE, in which the applied magnetic field is perpendicular to the surface of the sample and in the plane of incidence (refer to Figure 1.4). When the applied field is perpendicular to the plane of incidence and parallel to the sample surface it is known as transverse MOKE. In the case of longitudinal MOKE the applied magnetic field is parallel to both the plane of incidence and the sample surface. Each of these cases has their own applications and will be discussed separately [13].

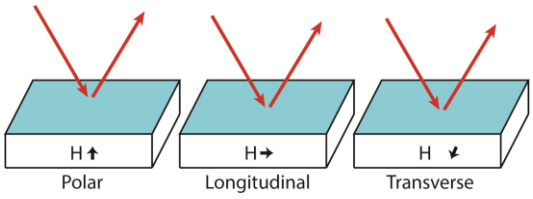

Figure 1.4. The three geometric configurations of MOKE

Polar SMOKE, where the applied field is perpendicular to the surface and parallel to the plane of incidence, has several useful advantages. To reveal them one must first determine a value for the total rotation by examining the simplified reflection coefficients:

$$r_{sp} = r_{ps} = \left[-\frac{4\pi}{\lambda}\frac{n_1 \cos\theta_2 \cos\theta_0}{(n_0 \cos\theta_0 + n_s \cos\theta_2)(n_0 \cos\theta_2 + n_s \cos\theta_0)}\right]\left[n_0 n_1 Q d \frac{M_p}{|M|}\right] \quad (1.14)$$

where *d* is the thickness of the film [9], and M_p is the polar component of the total magnetization, *M*. The equation is simplified by the geometry and calculated using Equation (1.11). Now it is possible to obtain the total Kerr rotation by combining Equations (1.12) and (1.14) and substituting into Equation (1.9), yielding a total Kerr rotation for polar geometry of

$$\varphi_p = \left(-\frac{4\pi}{\lambda}\frac{n_0 {n_1}^2 Q d}{(n_0 - n_s)}\frac{M_p}{|M|}\right) \quad , \quad (1.15)$$

where here φ_p represents the total polar Kerr rotation. There are several important aspects to note. First, the rotation depends on the square of the index of refraction of the magnetic material (n_1). This produces a large signal, making it very sensitive. The second thing to notice is that the rotation is independent of the angle of incidence (see Figure1.4). This allows for the experiment to be performed at any angle, including near-normal-incidence.

The next important configuration is longitudinal SMOKE, where the applied field is in the plane of the film and parallel to the plane of incidence (see Figure 1.4). In the thin film limit the reflective coefficients reduce to

$$r_{ps} = \left[-\frac{4\pi}{\lambda}\frac{n_0 n_1 \cos\theta_0 sin\theta_1}{(n_0 \cos\theta_0 + n_s \cos\theta_2)(n_0 \cos\theta_2 + n_s \cos\theta_0)}\right]\left[n_s Q d \frac{M_L}{|M|}\right] \quad (1.16)$$

and

$$r_{sp} = -r_{ps} \quad , \tag{1.17}$$

where M_L is the longitudinal magnetization. Again the total rotation can be calculated by applying Equation (1.9) yielding a total longitudinal rotation of

$$\varphi_L = \left(-\frac{4\pi}{\lambda}\frac{n_s Q d\ \theta}{(1-n_s)}\frac{M_L}{|M|}\right) \quad , \tag{1.18}$$

where θ is the angle of incidence. Examining Equation (1.18) shows that it is independent of the index of refraction of the magnetic material. In this arrangement it can be useful to choose a substrate in order to optimize the longitudinal signal (n_s near one). The next important note is that it is linearly dependent upon the angle of incidence (as measured from the normal). This means that the signal can be increased by increasing the angle, and that it cannot be measured near normal incidence.

The final configuration is transverse SMOKE, in which the applied field is in the plane of the sample, but perpendicular to the plane of incidence. Since there is no component of the light parallel to the magnetization, there is no rotation produced. Even though rotation is not measurable in this setup, for p-polarized light there is a small change in reflectivity, which depends on the direction of the magnetization of the sample [13].

1.4 Pulsed Laser Deposition

The synthesis of thin films in recent years has become imperative in the advancement of many areas of materials, physics, and technology, from the fabrication of devices to studying low-dimensional effects. There are many techniques used for the creation of thin films, each having their respective advantages and disadvantages. Some techniques include molecular beam

epitaxy (MBE), electron beam deposition, sputtering, chemical vapor deposition and many others. For highly complex crystal structures with several molecular components such as alloys, many deposition techniques are quickly ruled out. Techniques such as MBE and electron beam deposition work well for simple systems, but for materials with higher complexity and more molecular components these methods can have difficulty producing stoichiometric films. Chemical vapor deposition, although capable of depositing complex structures, is volatile due to high heat and harsh atmosphere, which limits its uses for many materials and substrates [14].

Pulsed laser deposition (PLD), although having its own limitations, offers several advantages for growing thin films. First, PLD often facilitates a congruent transfer of the target material to the substrate, a characteristic that is more difficult to attain using other techniques such as e-beam deposition or thermal evaporation. Second, PLD is able to produce a large range of ionic energies. As the ions in the plasma plume reach the substrate, they have an energy between 0.1-100 eV, depending on the deposition parameters, which spans the optimum range for many systems. This higher ion energy enhances reactivity and ordering on the substrate, although it can also embed particles in the surface. Compared to MBE and thermal evaporation, which have energies on the order of 0.1 eV, PLD is much more versatile. Third, PLD is usually performed in UHV environments which allows for minimal contamination and a high degree of purity in the film growth. Fourth, PLD can be done in reactive atmospheres, such as oxygen or nitrogen, which allows for the uniform deposition of various oxides or nitrides. Finally, epitaxial growth of films can be achieved through a careful tuning of the plume characteristics and deposition parameters [14].

In 1965 Smith and Turner were the first to successfully manufacture thin films using a high powered ruby laser [15]. The original technique was crude compared to contemporary PLD

systems and depended on continuous wave lasers. In the mid-1970's, with the invention of electronic Q-switches, the production of very short, high-energy, pulsed lasers made laser deposition more reliable. Not until 1987 did PLD become a popular technique for fabricating thin films. It was the manufacturing of high T_c superconducting films by Venkatesan that spurred the newfound interest [16]. Since then, the availability high-power, pulsed lasers, and the improved quality of growth has elevated PLD to become a prevalent technique in material science.

Pulsed laser deposition is now a well-developed, versatile technique employed to grow highly-crystallized, multicomponent thin films. The simplest setup uses a high-energy excimer laser and an ultra-high vacuum (UHV) chamber. Using optics designed specifically for ultra violet (UV) light, aligning and steering the laser can be straightforward. Focusing lenses are used to decrease the area of the laser spot thus increasing the fluence and intensity. Care must be taken when choosing the material for the chamber window to insure minimal loss of transmission. Materials such as magnesium fluoride, sapphire, and UV-grade fused silica are quality UV transmitters.

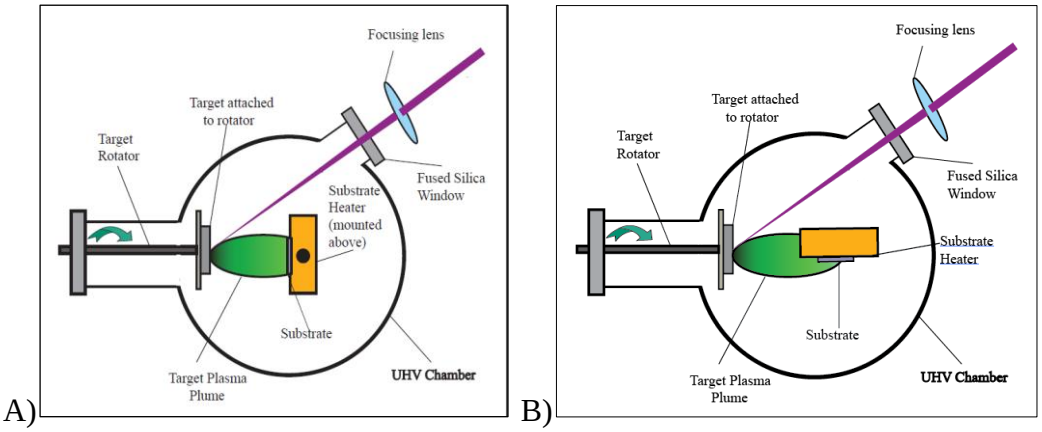

Figure 1.5 The basic configuration for PLD. The incoming laser strikes the rotating target producing a plasma plume that will condense on the substrate. The target rotates to evenly ablate the surface. (A) In on-axis deposition, the substrate is perpendicular to the plume axis, (B) In off-axis PLD, the substrate is placed parallel to the plume axis. [14]

Once the laser has been aligned, the beam strikes the surface of the target. The interaction at the surface can be quite complex and highly dependent upon the material. Sufficiently high fluences must be used to achieve desired deposition rates. Fluences, defined as the energy per pulse divided by the spot area, on the order of 5 J/cm^{-2} are usually needed for metallic samples. With a laser pulse of 20 ns this gives a power density of 0.25 GW/ cm^{-2}. The target material is ejected from the surface of the target in a plasma plume oriented normal to surface of the target as shown in Figure 1.5 (A). The plasma plume, composed of many types of ionic and neutral species, can interact with an ambient reactive gas along its path to (and at) the substrate. Upon arrival, the plasma will condense on and react with the substrate, creating a uniform thin film; the substrate is usually heated since the substrate temperate can greatly affect the types of reactions that occur and the structural quality of the film.

The traditional configuration for PLD (Figure 1.5 (A)), where the substrate faces the target (i.e., the plume impinges at normal incidence upon the substrate), has some advantages and disadvantages. One advantage is a maximized growth rate. One disadvantage that occurs in the deposition of some materials is particulate formation. Particulates are unwanted since they disrupt film formation and are generally intrusive, off-stoichiometric impurities. Particulates can be minimized in a number of ways. First, since these particulates are essentially tiny, ejected pieces of the target, they are much slower than the rest of the plume, which are composed of much lighter ions and neutrals. By placing the substrate further from the target and in different positions within the plume, the particulates may be reduced. One can also use a rotating velocity selector (essentially a turbo-pump-style rotating vane system): since the particulates are moving

slower, they are less likely to pass through the high speed vanes [17]. Velocity selectors are difficult to implement and are seldom used.

Another method that is easy to employ is off-axis PLD. In this configuration (see Figure 1.5 (B)), the substrate is oriented perpendicular to the target (parallel to the plume axis). At first glance this seems as if it would not produce the adequate growth rates required, but the presence of an inert or reactive gas helps facilitate film growth [18]. While the on-axis deposition is most often done near UHV pressures (10^{-8} to 10^{-10} torr), off-axis deposition uses a background gas (on the order of 10^{-1} to 10^{-2} torr) to produce a scattering effect. The process is much slower and can be more difficult to align, but can produce highly uniform and epitaxial films. The atmosphere is highly controlled, and through varying pressure and gas type, one can fine-tune the growth parameters. Argon is often used for non-reactive deposition. In addition to non-reactive gasses, a reactive atmosphere may be used, such as oxygen, to create uniform oxide films [18,19].

PLD can be used extensively for small-scale laboratory applications, but is limited in regard to large-scale industrial uses. One benefit of using PLD in the lab is it is extremely versatile. Though the on-axis and off-axis depositions may require different chambers, one laser can be employed with several chambers through the use of mirrors and beam splitters. It would seem that such a useful technique would be preferred for large scale industry, but PLD has limitations. A significant problem in scale-up is the plume distribution, which is large enough for individual films, but far too small for most industrial uses. [18]

1.5 Full-Heusler Alloys

The next evolutionary step in electronics, spin-electronics (or *spintronics*), has been the cornerstone in the explosion of technological applications ranging from computers to communications. Spintronic devices use a combination of ferromagnetic, antiferromagnetic, ferromagnetic, non-magnetic, and semiconducting materials to produce devices that exploit not only charge, but also electron spin (even quantum and interference effects). Such devices are becoming more important and can be found in magnetic random access memory (MRAM) and magnetic hard drives. In many cases advancement is dependent upon the materials available in this field. Half-metallic, full-Heusler alloys have been researched for years and are of great potential in advancing the field of spintronics [20-23].

In order to understand spin-polarized materials it is important to review some fundamental magnetic phenomena of materials. All materials, when placed in an applied magnetic field, will produce a small magnetic field that opposes the applied field. This phenomenon is known as diamagnetism. Although all materials show some form of diamagnetism, the strength of the induced magnetic field is normally small. This is seen in the small negative magnetic susceptibility, which is largely independent of temperature [24].

Paramagnetism often plays a more important role in materials. Contrary to diamagnetism, a paramagnetic sample will produce a magnetic field parallel to the applied magnetic field. This phenomenon occurs in materials that have atoms with a net magnetic moment, although, due to thermal effects, the net moment will be zero in zero applied field. An applied field will induce an average alignment with the applied field, yielding a net magnetization in the same direction as the applied field. When all of the magnetic moments are aligned with the applied field, the

sample will have a maximum magnetization referred to as the saturation magnetization, M_s. In most samples the paramagnetic signal will be an order of magnitude larger than the diamagnetic signal, essentially washing out any sign of the diamagnetism. Curie showed that the paramagnetic signal is generally proportional to the inverse of temperature, which became known as Curie's law [24]. Although both diamagnetism and paramagnetism are present in most samples, the signal is small when compared to the magnetic signal of ordered magnetism.

There are several types of ordered magnetism that are of interest: ferromagnetism, antiferromagnetism, ferrimagnetism, and helical magnetism. Although this thesis will focus on ferromagnetic samples, a brief discussion of the others will be of value.

Neither diamagnetism nor paramagnetism is the results of moment-moment interactions, but due to interactions with an external applied field. Ferromagntism is characterized by a spontaneous magnetization even in the absence of an external magnetic field. This is a form of ordered magnetism, which is caused by the direct or indirect intaction between neighboring magnetic moments. There are several forms ordered magnetism including ferromagnetism, antiferromagnetism, ferrimagnetism, and helical magnetism, all of which result from the various types of interactions between neighboring moments.

Ordered magnetism must be mediated by an interaction between neighbors. The most intuitive interaction is direct exchange, where the nearest neighbor orbitals interacting directly with one another. This usually cannot account for ferromagnetic order, since the range of direct exchange is small, allowing for little or no overlap between the orbitals. This means that the interaction responsible for most forms of ferromagnetism must be mediated by some other phenomenon.

Since direct exchange is too weak for ordered magnetism, the interaction must be an indirect exchange between the magnetic sites. There are several kinds of indirect exchange interactions. The first is the superexchange in which the interaction between magnetic sites is mediated by another atom, in most cases non-magnetic atom. A simple example is MnO, which antiferromagnetic. Since the oxygen only has two free states for the Mn to bond, it will for two single bonds with the neighboring Mn. Due to the Pauli exclusion principle the two electrons must be of opposite spin. This will yield a system in which it is energetically favorable for the electrons of the Mn to align antiparallel. This produces equal and opposite magnetic moments, thus producing antiferromagnetism. In other systems it is favorable for the magnetic moments to align parallel, yielding ferromagnetic ordering. Superexchange is the main interaction which causes ferromagnetism in the Heuler alloys studied in this thesis. [25]

The second indirect exchange interaction is found in metals. The superexchange uses an intermediate atom to mediate the interaction between magnetic atoms, but in the case of the Ruderman, Kittel, Kasuya, and Yosida (RKKY) interaction, (itenerate exchange) this is not the case. In the RRKY interaction the conduction electrons facilitate the interaction [26]. A local magnetic moment will spin-polarize the conduction electrons, which will in turn couple to neighboring magnetic moment. The RKKY interaction has a cosine dependence based on the radius of the Fermi surface and the distance between magnetic moments. This means that the interaction can yield either a ferromagnetism or antiferromagnetism based on the distance between magnetic moments.

When the exchange interaction favors the antiparallel alignment there are two possible cases. In the case of antiparallel alignment the net interaction can be viewed as a superposition of two sublatices pointing in opposite directions. If the magnetizations of the two sublatices are

equivalent, then antiferromagnetism is produced. Antiferromagnetism is characterized by the absence of any net magnetization (at least in the ideal case). When the magnetizations of the subatices are different, ferrimagnetism will result in a net permanent magnetization. The net result is a smaller moment than either individual sublattice.

In a ferromagnet, the spin up and spin down electrons will have a different mobility, i.e. the current can contain a higher distribution of either spin up or spin down electrons. This is highly dependent upon the degree of spin-polarization of the ferromagnetic material used. The spin-polarization is given by the difference of the spin up and spin down electrons over the sum of both spins.

$$P = \left|\frac{n_\uparrow - n_\downarrow}{n_\uparrow + n_\downarrow}\right| \tag{1.19}$$

where $n_\uparrow$ is the number spin up electrons and $n_\downarrow$ is the number of spin down available at the Fermi level. For the case P=1 the material is entirely spin-polarized, meaning there is a band gap at the Fermi level for one spin while there is a finite density of states at the Fermi level for the other. These materials are known as half-metals. They are of particular interest in spintronics for several reasons. Half-metals can be used as a spin filter since only one spin has a conduction band. This means they can be used for devices such as magnetic tunnel junctions, spin-transistors, magnetic random access memory (MRAM), etc. [20, 22].

There are several types of materials that are predicted to be half-metals, but the ones that are most often of interest are the Heusler series compounds. The first theorized half-metal was NiMnSb, theorized in 1983 by de Groot [27], although the name is given to the chemist Friedrich Heusler who first discovered the structure type in 1903 [25]. There are two types of Heusler compounds, half-Heusler, which are of the form XYZ, and full-Heusler, of the form X_2YZ. The interest in these materials stems from the high degree of polarization and diversity in

composition. Although X often represents a magnetic element: X= Fe, Co, or Ni, other transition elements can be used such as Rh, or Ru. Although Y is most often Mn, it can also represent Fe or Cr. Z is given by a wide range of transition metals and semiconducting elements.

Of these two types of Heuslers, the full-Heusler compounds are of particular interest. They contain a wide range of interesting electronic behavior in addition to the high degree of spin polarization. The full-Heuslers have the $L2_1$ crystal structure which is characterized by four face centered cubic lattices.

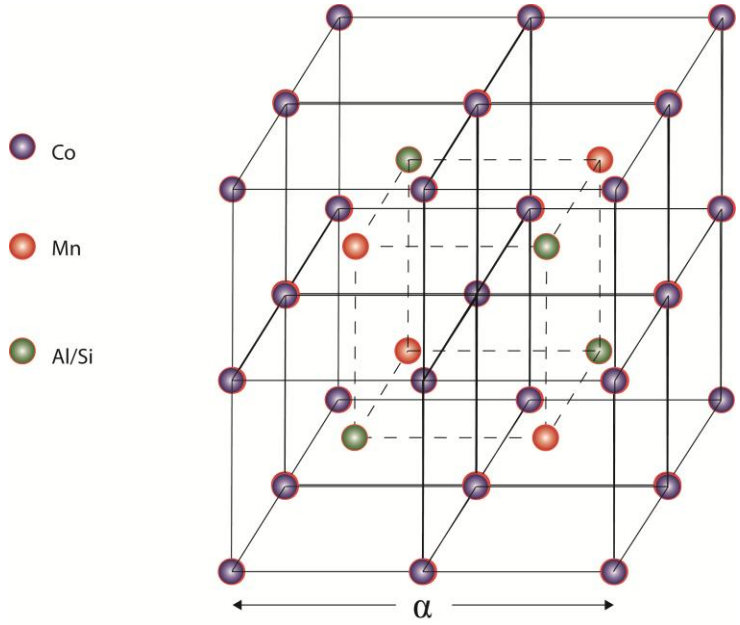

Figure 1.6 The $L2_1$ structure is characterized by four fcc sublattices.

A great deal of research has been done on these materials [28-42]. This thesis will focus on a series of $Co_2MnSi_xAl_{1-x}$ films deposited using pulsed laser deposition. There have been extensive theoretical calculations done on this material, but many of these calculations are still to be confirmed by experiment [31-38]. The Co_2MnSi, a full-Heusler alloy, is expected to show a magnetic moment near 5 μ_B. Co_2MnAl, which is also a full-Heusler alloy, should yield a magnetic moment of 4 μ_B [6]. This is expected since we are doping electrons into the series, thus

moving the Fermi energy. Both materials are predicted to be highly spin polarized [39], although this has not been realized in experiment. The interest of this thesis is to further understand the experimental properties of this series by finding the magneto-optic Kerr effects as a function of the doping levels of Al and Si.

Chapter 2
Experimental MOKE

2.1 Experimental Setup

John Kerr's original experimental setup used the best optics available to observe the total Kerr rotation, but he was unable to quantify the total change in rotation and ellipticity. Using a modern analog of Kerr's original experiment, measurements of the total Kerr rotation can easily be achieved. The current optical setup employed in this study replaces the Nicol prisms with Glan-Thompson prisms with an extinction ratio of 100,000:1, producing highly polarized light. The light source has been changed to a 640 nm Obis diode laser instead of a paraffin source. Kerr's electromagnet was able to use a large current to create a magnetic field, which could be switched by changing the direction of the current. The magnet used in this experiment is an electromagnet attached to a bipolar power supply. This power supply is controlled by a general purpose interface bus (GPIB) controlled by a computer. This allows for fine and continuous control over the applied magnetic field. Using a Gaussmeter attached to the computer via GPIB cable, the applied magnetic field can be accurately measured. Although *in situ* measurements of the applied field are within the capabilities of the system, the accuracy can be diminished due to the placement of the detector. Instead a calibration table was constructed. By placing the probe of the Gaussmeter in place of the sample and recording the magnetic field versus the applied voltage, one can create an accurate representation of the magnetic field at the sample surface.

The samples were placed in the center of the applied field on a rotator that allows for the sample surface to be rotated 360 degrees with respect to the plane of incidence. The particular sample holder used here has increments of approximately five degrees. Kerr was able to observe the rotation induced by the sample and roughly compare them to each other based on the change in brightness seen after the analyzer. Using modern photo detectors one can now accurately

measure the change in intensity of the light. This experiment uses a Hinds photodiode detector. The voltage from the detector is read using a nanovoltmeter, which is then recorded by the computer using a GPIB interface and a LabView control program. This allows for the change in intensity to be measured in tandem with the change in applied magnetic field.

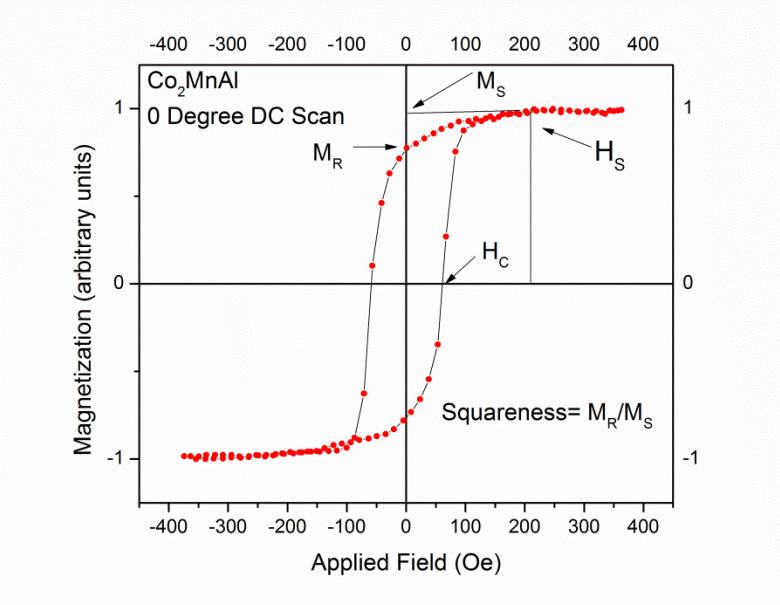

Figure 2.1 The hysteresis loop showing the coercive field, the saturation field, the remnant magnetization and the saturation magnetization.

A custom LabView program recorded the data from the detector and creates a plot of voltage versus applied field. As shown in Equation (1.18) the total Kerr rotation is linearly dependent upon the magnetization. Taking advantage of this relationship the plot of voltage versus applied field can be interpreted as the relative magnetization versus applied field (MvH) hysteresis loop. Although the absolute magnetization cannot be determined from this relationship, the coercive field, saturation field, and squareness of the material can easily be obtained, as shown in figure 2.1. Since the sample can rotated, the same measurements can be taken at several angles of the sample with respect to the plane of incidence. The easy and hard axis can be obtained from these rotations. For a magnetically anisotropic sample, the easy axis is

defined as the axis which is energetically favorable to magnetize [24]. If the data is taken for small increments, one can create a polar plot of the coercive field or saturation field as a function of the angle [29], giving insight into the magnetic anisotropy of the sample.

This technique uses only the DC signal from detector to create a hysteresis loop and is known as DC-MOKE. It is a useful technique that can yield important information by taking advantage of MOKE, but does not separate the Kerr rotation and ellipticity. To measure the Kerr rotation and ellipticity additional optical components and electronics are needed. Using a method known as AC-MOKE, one can determine the values of the Kerr rotation and ellipticity for a given sample. By using a photoelestic modulator (PEM) as an oscillating retarder, one can create an AC signal that can be read by a lock-in amplifier. By analyzing the AC intensity using Jones matrix analysis, it can be shown that the Kerr rotation and ellipticity can be measured separately.

Figure 2.2 shows the optics table in conjunction with the electronics used to take the measurements. Although there are several configurations in which one can measure the Kerr rotation and ellipticity, in this thesis two variations are used. The PEM is placed between the sample and the analyzing polarizer. Both the PEM and the analyzer are free to rotate 360 degrees. A Jones matrix analysis was used to determine the optimal angles for the PEM and analyzer.

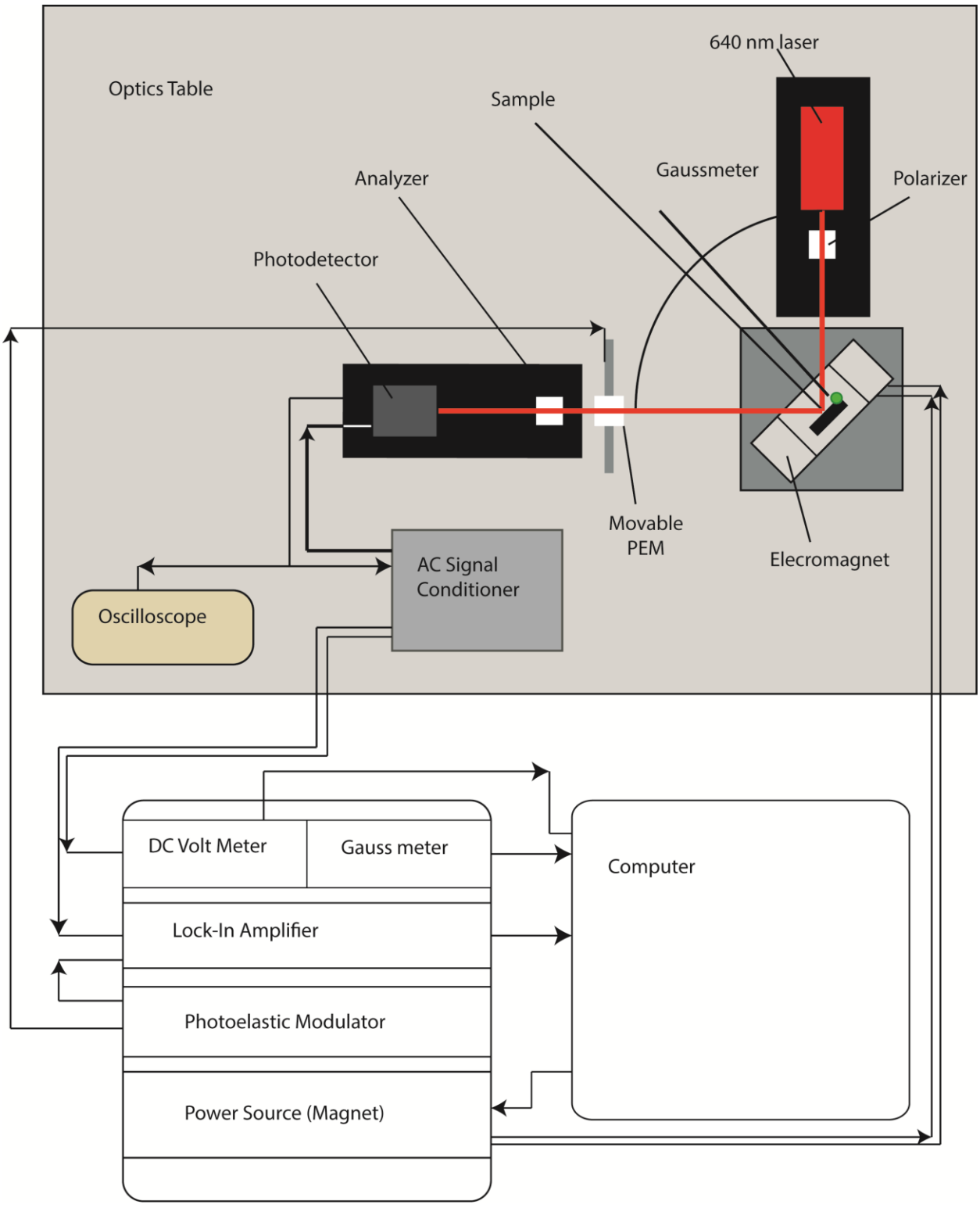

Figure 2.2 The schematic for the basic optical and electronic setup, showing all components and connections.

2.2 Jones Matrix Analysis

Jones matrix analysis uses a matrix representation for the optical elements of the experiment to determine the theoretical intensity at the detector. It can be broken into its components to show the separate the individual components of the intensity. This is important because, using a lock-in amplifier, the signals can be separated and individual terms can be measured.

The matrix analysis begins with a matrix representation of the electric field vector of the incident light in terms of p- and s- polarized light:

$$E = \begin{pmatrix} E_p \\ E_s \end{pmatrix}. \tag{2.1}$$

Equation (2.1) represents the most general electric field emitted by the light source. The light will then continue and pass through the polarizer, which is represented by the Jones matrix

$$P = \begin{pmatrix} cos^2(\beta) & sin(\beta)cos(\beta) \\ sin(\beta)cos(\beta) & sin^2(\beta) \end{pmatrix}, \tag{2.2}$$

where β is the angle between the plane of incidence and the plane of polarization. The resulting linearly polarized light will reflect from the surface of the sample.

The interaction at this surface is that will produce the measured effects must also be represented a matrix. The sample surface is characterized by

$$S = \begin{pmatrix} r_p\, e^{i\delta_p} & r_{ps}e^{i\delta_{ps}} \\ r_{sp}e^{i\delta_{sp}} & r_s e^{i\delta_s} \end{pmatrix}, \tag{2.3}$$

where $r_{ps}\, e^{i\delta_{ps}}$=-$r_{sp}\, e^{-i\delta_{sp}}$. The phase angle of the electric field is specified by δ_i. Equation (2.3) is equivalent to the matrix representing the Fresnel reflection as shown in Equation (1.8). The diagonal terms are independent of the magnetization of the sample, but the off-diagonal are sensitive to the Kerr effect [8].

The AC technique is designed around the functionality of a photoelastic modulator (PEM), which generates a periodic retardation at a frequency of 50 kHz. The interaction with the electric field is denoted by the matrix

$$R = \begin{pmatrix} e^{i\varphi/2} & 0 \\ 0 & e^{-i\varphi/2}) \end{pmatrix}, \tag{2.4}$$

where φ represents the periodic retardation where the time dependence is written as

$$\varphi = \varphi_0 \sin(\omega t), \tag{2.5}$$

where φ_0 represents the phase amplitude of the PEM. In order to express this in a form that is useful for experiment, a Fourier decomposition must be done to determine cos($\varphi(t)$) and sin($\varphi(t)$). Doing so yields

$$\cos(\varphi(t)) = J_0(\varphi_0) + 2\sum_{m=1}^{\infty} J_{2m}(\varphi_0)\cos(2m\omega t), \tag{2.6}$$

and

$$\sin(\varphi(t)) = 2\sum_{m=0}^{\infty} J_{2m+1}(\varphi_0)\sin((2m+1)\omega t), \tag{2.7}$$

where J_k is the Bessel function of order *k* and a function of the phase amplitude. Finally the light passes through the analyzer before reaching the detector. The analyzer (a second polarizer) is characterized similarly to the first polarizer:

$$A = \begin{pmatrix} cos^2(\alpha) & sin(\alpha)cos(\alpha) \\ sin(\alpha)cos(\alpha) & sin^2(\alpha) \end{pmatrix}, \tag{2.8}$$

where α is the angle between the polarization and the plane of incidence.

Calculating the reflected electric field can now be done by multiplying the above matrices in the correct order:

$$\begin{pmatrix} E_p \\ E_s \end{pmatrix}^r = ARSP \begin{pmatrix} E_p \\ E_s \end{pmatrix}^i , \tag{2.9}$$

where *i* and *r* represent the incident and reflected electric fields. Since the intensity is what is measured and not the electric field, it is important to note that $I \propto |E^r|^2$. Using this method it is straightforward to determine the expected signal for various angles of the polarizer, the PEM, and the analyzer [13, 43,44]. Although the angle of the polarizer would be easy to manipulate with these equations, s-polarized light ($\beta = 90°$) is assumed throughout the analysis.

Before continuing through the signal analysis it would be useful to define the Kerr rotation and ellipticity in terms of the Stoke's vector components [39, 43,44] (assuming s-polarized light):

$$I = {r_s}^2 + r_{ps}^2$$

$$Q = {r_s}^2 - r_{ps}^2 \tag{2.10}$$

$$U = 2r_s r_{ps} cos\left(\delta_s - \delta_{ps}\right)$$

$$V = 2r_s r_{ps} sin\left(\delta_s - \delta_{ps}\right)$$

where again r_i is the component of the Fresnel reflection matrix and δ_i is phase angle as discussed in equation (3). In terms of the Stoke's vector, the ellipticity and the rotation of a general polarized beam are defined as

$$\epsilon = tan[\tfrac{1}{2}\ sin^{-1}\left(\tfrac{V}{I}\right)] \approx \tfrac{1}{2}\tfrac{V}{I} = \tfrac{v}{2}, \tag{2.11}$$

And

$$\theta = \tfrac{1}{2}tan^{-1}\left(\tfrac{U}{Q}\right) \approx \tfrac{1}{2}\tfrac{U}{Q} = \tfrac{1}{2}\tfrac{u}{q}, \tag{2.12}$$

where $q= Q/I$, $u=U/I$ and $v=V/I$ [14, 43]. The small angle approximation has been applied to the exact equations. This assumption is valid in the case of the Kerr effect because the changes in rotation and ellipticity are small. Also for the case of the Kerr effect, it can also be assumed that the change in intensity is small (r_{ps}^2 is small), yielding $I \approx Q$, or q=1. This gives the value for Kerr rotation and ellipticity as

$$\theta_k = \frac{u}{2} \qquad \text{and} \qquad \varepsilon_k = \frac{-v}{2} \tag{2.13}$$

Now that the Kerr rotation and ellipticity are defined, one can analyze and interpret the intensity. There are two sets of angles of the PEM and analyzer used in this experiment. In first setup the PEM is placed at 0° and the analyzer at 45°. Again, assuming s-polarized light, Equation (9) yields

$$I \propto \tfrac{1}{2}r_s^2 + \tfrac{1}{2}r_{ps}^2 + J_0(\varphi_0)r_s r_{ps}\cos(\delta_s - \delta_{ps}) + 2J_1(\varphi_0)r_s r_{ps}\sin(\delta_s - \delta_{ps})\sin(\omega t) + 2J_2(\varphi_0)r_s r_{ps}\cos(\delta_s - \delta_{ps})\cos(2\omega t) + \cdots \tag{2.14}$$

Equation (1.14) only takes the first few terms of the Fourier series since the higher order terms are negligible. By applying equations (1.11) and (1.12) and defining the term $I_0 = \frac{1}{2}r_s^2 + \frac{1}{2}r_{ps}^2$ (or the DC intensity), equation (1.14) can be put in terms that are most commonly found in the literature:

$$I = I_0[1 - 4\varepsilon_k J_1(\varphi_0)\sin(\omega t) + 4\theta_k J_2(\varphi_0)\cos(2\omega t) + \cdots], \tag{2.15}$$

where the phase amplitude has been chosen to minimize the value of the J_0 term, making it negligible. The J_0 term is zero at $\varphi_0 \approx 2.405$ radians. Examining Equation (2.15) shows that the rotation and ellipticity terms have been separated and, more importantly, are related to the intensity by the second and first harmonics, respectively, meaning a lock-in amplifier will isolate them in separate measurements. Using a signal conditioner, one can separate the AC signal form the DC signal, and allow them to be measured in tandem.

Although this optical arrangement will allow for the measurement of both the rotation and the ellipticity, experimentally, the background noise is significant in the case of the first harmonic, making it difficult to measure the ellipticity. By separating the intensity of the second harmonic using the lock-in amplifier, the Kerr rotation can be isolating and calculated using

$$\theta_k = \frac{\sqrt{2}}{4J_2}\frac{V_{2f}}{V_{DC}}, \tag{2.16}$$

where V_{2f} is the voltage read by the lock-in (of the second harmonic), V_{DC} is the DC voltage, and J_2 is the second order Bessel function, and the factor of $\sqrt{2}$ comes from the fact that the lock-in measures V_{rms} instead of the peak voltage.

The calculation of the Kerr rotation has one major difficulty. Although the voltage is the measured value, the calculation is in terms of the intensity. The detector does not have a one to one ratio of intensity to voltage. There are always losses in the detector due to several sources. The first main source is a DC dark current. This effect is inherent to the detector and can depend on the ambient temperature. A stable temperature can help keep the dark current stable. The dark current in the photodiode used in this experiment is low and not a real issue here. The second source of loss comes from electrical offsets in the electronics. This can often be directly correlated with a DC offset that can be adjusted to zero out the voltage (this offset can also take into account the dark current). The final source of loss is the ambient light associated with the optical setup. Any light reaching the detector will cause some voltage including those that are not associated with the experiment. Since this experiment uses a monochromatic laser, the easiest way to remove ambient light is the use of a bandpass filter. Additional light can be removed using a shielding around the detector with a narrow aperture.

Even after minimizing the electrical offsets, it is important to be able to measure the ratio of intensities to the ratio of the voltages. There should be a constant of proportionality relating these two rations according to the relationship

$$\frac{I_{AC}}{I_{DC}} = K_2 \frac{V_{AC}}{V_{DC}}. \tag{2.17}$$

By changing the optical setup slightly (see Figure 2.3), the ratio of the voltages can be measured and then compared directly to the theoretical value of the intensity for the arrangement [45]. Once the value for K_2 has been determined, it can be add taken into account in Equation (2.16)

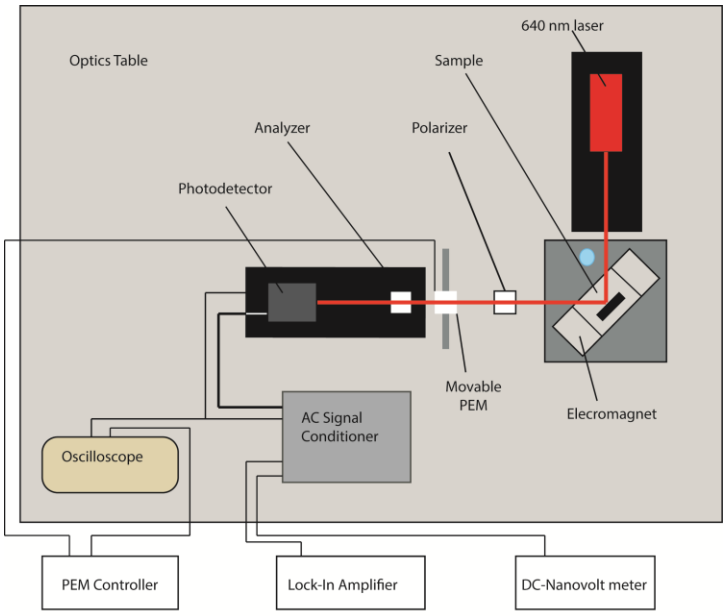

Figure 2.3 The optical Arrangement to measure the value of K_1 uses a mirror in place of the sample and places the polarizer and analyzer at 45˚and -45˚, respectively, with the PEM placed between [45]. One then measures the ratio of the voltages directly, which can then be compared to the theoretical value.

The theoretical calculation for this optical arrangement is quite straightforward. The total intensity is given by

$$I = \frac{I_0 K_2}{2}[1 - \mathrm{Cos}(\varphi_0 \cos(\omega t))]. \tag{2.18}$$

To separate the AC and DC intensity one must calculate a Fourier series decomposition, which yields

$$I = \frac{I_0 K_2}{2}[1 - J_0(\varphi_0) + 2J_2(\varphi_0)\cos(2\omega t)] \tag{2.19}$$

As before, the phase amplitude φ_0 can be set to 2.405 radians to minimize the effect of the J_0 term. This results in the ratio of the intensities being given by

$$\frac{I_{AC}}{I_{DC}} = 2J_2(\varphi_0)\ . \tag{2.20}$$

After taking measurements and comparing, this resulted in a value of K_2 =1.3 for the current system. Although several measurements were taken and averaged, the variations in temperature and ambient light were the main obstacles making precise measurements. Now that the value of K_2 has been measured, one can calculate accurate values of the Kerr rotation using Equation (2.15).

Accurate values of the ellipticity are slightly more difficult to obtain. As pointed out above, the same arrangement used to measure the rotation can be used, but the signal to noise ratio for this setup is not the optimal as pointed out by Polisetty et al.[46]. The best signal to noise ratio for the first harmonic comes in the case of the PEM being placed at an angle of 45˚ and the analyzer at an angle of 0˚. This gives a signal to noise ratio that is nearly twice that of the first setup. This is very important because the signal for the first harmonic in the case of our measured values is small. For this configuration, the Jones matrix analysis gives an intensity of

$$I \propto \frac{1}{2}r_s^2 + \frac{1}{2}r_{ps}^2 + \frac{1}{2}J_0(\varphi_0)(r^2{}_s - r^2{}_{ps}) + 2J_1(\varphi_0)r_s r_{ps}\sin(\delta_s - \delta_{ps})\sin(\omega t) + 2J_2(\varphi_0). \tag{2.21}$$

It is readily apparent that the J_1 term is the same as in Equation (2.14), but the J_2 term is not. This means that the ellipticity can be calculated according to the same equation as it would be if using Equation (2.15):

$$\varepsilon_k = \frac{\sqrt{2}}{4J_1}\frac{V_{1f}}{V_{DC}}, \tag{2.22}$$

where V_{1f} is the AC voltage of the first harmonic measured by the lock-in amplifier. Again the value for K_2 can be used to account for electronic offsets.

2.3 Experimental Procedure

The goal of this thesis was to setup an AC MOKE system in order to measure the Kerr rotation and Kerr ellipticity of ferromagnetic thin films. Initial measurements of the Kerr rotation and ellipticity were taken on a series $Co_2MnSi_xAl_{1-x}$ deposited on GaAs, using on-axis PLD.

The $Co_2MnSi_xAl_{1-x}$ series included five bulk targets with concentration values of x= 1, 0.75, 0.50, 0.25, and 0.00. The GaAs substrates were annealed in the chamber (at P$\approx 1x\,10^{-8}$ torr) at 600℃ for 15 minutes, and the temperature was reduced to 240℃ for the deposition. Several deposition temperatures were tested (25℃, 200℃, 240℃, 400℃, and 600℃), but the best quality films were grown at 240℃. The excimer laser used was a KrF laser with a wavelength of 248 nm. The laser was run at a rate of 10Hz and an energy of 350 mJ/pulse. This resulted in a uniform films of nominal thickness. The substrate was adhered to the holder using silver paste, which loses integrity at temperatures near 600℃. To compensate, the substrate was held down using a thin piece of metal screwed into the substrate holder. The metal strip resulted in a clean section of the substrate, which could be used as a step edge to measure the thickness with atomic force microscopy (AFM).

After the deposition, the sample was allowed to cool to ambient temperature before removing from the chamber. Once removed, the sample was quickly mounted to the MOKE sample holder. This was done in two separate ways. The first used double sided carbon tape to hold the sample in place. This did not work well because alignment of the sample was difficult and the carbon tape would lose its adhesive properties after only a few samples, which could result in the film falling from the holder in the middle of measurements. The GaAs substrates are brittle and a short fall could result in damage to either the film or the substrate. The second

method used vacuum grease. By placing a small amount of N-type grease on the end of the sample holder, the sample was held in place and could easily be moved for alignment. Care had to be taken to make sure no grease was transferred to the surface of the film. Once on the surface, the grease cannot be effectively removed without damage to the film. Care must also be taken to keep the sample clean of fingerprints for the same reason.

Once mounted on the sample holder, the sample was placed in the center of the magnet. (Caution should be taken to make sure the power to the magnet is turned off when working near it.) The laser used was a variable power OBIS 640 nm diode laser. It was operated at a power of 8 mW (experimentally determined to facilitate the use of higher amplitude gains and to not saturate the detector). The reflected beam had to be carefully aligned to hit the center of the detector, since small variations resulted in unusable data.

Once aligned, for each sample DC-MOKE loops were measured at four different angles (0°, 45°, 90°, and 135°) with respect to the plane of incidence to confirm the quality of the films, and to get some basic information about the magnetic anisotropy. Using the angle that was closest to the easy axis, the PEM was put into place and then the AC-MOKE measurements were taken. Care was taken to make sure the PEM was set as close to 2.405 radians as possible, which was 2.407 radians for the current setup. This was close enough to 2.405 so the zero-order Bessel function was negligible. The lock-in amplifier settings were often the most import step in confirming the alignment for the AC-MOKE setup. The auto-phase option would automatically maximize the signal with reference to the PEM phase. Examining Equations (2.14) and (2.15) shows that the rotation is depends on the sine of the second harmonic, which is maximized at a phase of 90°. When auto-phasing, care was always taken to make sure the phase was correct, although the phase was expected to be a few degrees off since it was locking in on a square wave

pulse. When measuring the ellipticity, the first harmonic depends on the cosine, which is maximized at 0°. The lock-in also has an auto-gain feature that can be used in conjunction with the gain settings of the signal conditioner to find the optimal gain settings. This must be done separately for both the rotation and ellipticity. The last step before taking measurements is to set the reserve on the lock-in. Again there is an auto-reserve setting, that used in tandem with the filters that can help stabilize the measurement. Once all the settings are done, it is always good practice to auto-phase again to make sure that the signal is still in phase since even a simple bump of the optics table can knock the beam off the detector.

The LabView program that controls the experiment has an input setting for the gain settings of the signal conditioner and for the value of K_2 (Equation (2.17). The settings also allow for the number of points per graph and for the current range of the power source of the magnet. When taking data, the program is design to read the AC and DC voltages in tandem. It then records them in a data file and plots them on screen. It will then calculate the value of the Kerr rotation or ellipticity in a third plot. It can read the harmonic being measured from the lock-in amplifier and has been programmed to use the appropriate Bessel function required for the measurement. Each run is recorded in a separate data file, which can then be imported into a separate graphing program to analyze the data.

Chapter 3
Results and Discussion

3.1 DC-MOKE

The main objective of this thesis was to set up a reliable system to measure the magneto-optic Kerr effect of thin films. The extensive process began with the basic arrangement of the DC-MOKE, nearly mimicking Kerr's original experiment. The first measurements were taken on Co_2MnAl. While the parameters for the deposition were still being determined, the DC-MOKE was tested. The confirmation of the results of the hysteresis loops were confirmed using the magnetic properties measurement system (MPMS). Although this was only done for one sample it was able to give a calibration for the system, by comparing the shape and the coercive field of the hysteresis loop from the MPMS to the results of the DC scan. It showed that the DC-MOKE was accurate in terms of finding the coercive field. Although the AC-MOKE is the main focus of this thesis it is worth discussing the work done with the DC-MOKE since it was helpful in characterizing the Heusler alloys used.

For the $Co_2MnSi_xAl_{1-x}$ series, five targets were made using traditional arc-melting techniques. XRD was performed on the series to confirm the $L2_1$ structure and compare the lattice constant to the expected values (Figure 3.1). The lattice constants ranged from 5.61 Å for Co_2MnSi to 5.77 Å for Co_2MnAl [29]. For each target, two films were grown, yielding a total of ten films, each of approximately 500 Å. For each film, the DC-MOKE was measured for at least four separate angles followed by the AC-longitudinal MOKE using the methods described earlier. The DC measurements were used to gain insight into the magnetic anisotropy, remnant magnetization, saturation field, the coercive field and the squareness of the measured samples (see Figure 2.1). The main use of the DC-measurements though was to be able to compare the

two films of the same target to confirm that they had similar features and coercive fields. A quick comparison was able to show that the films produced similar hysteresis loops.

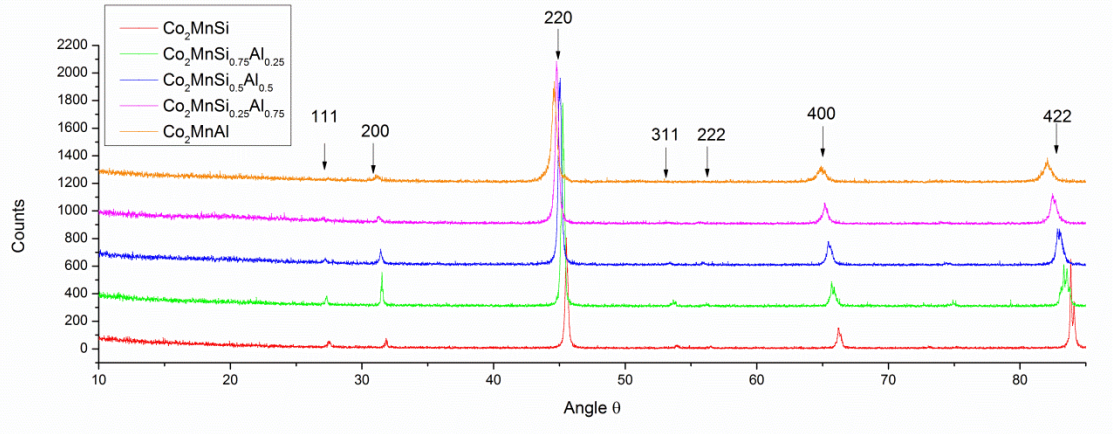

Figure 3.1. The XRD data for the $Co_2MnSi_xAl_{1-x}$ shows the $L2_1$ crystal structure with a lattice constant ranging from 5.61 Å for Co_2MnSi to 5.77 Å for Co_2MnAl. The data has been offset by 300 counts.

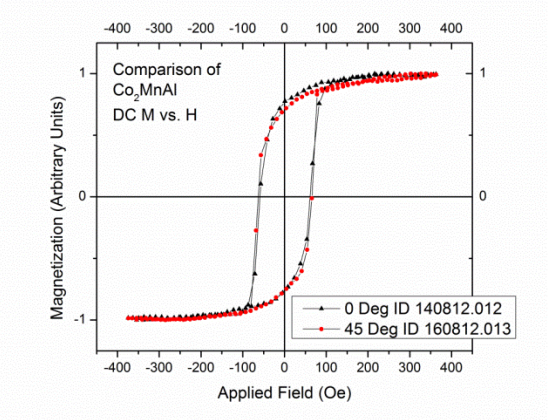

Figure 3.2. It was important to compare the two films of the same composition to confirm that they had similar features and to align the films. The comparison between the 0° orientation of the first Co_2MnAl film and of the 45° orientation of the second Co_2MnAl film reveals similar hysteresis loops.

To measure the hysteresis loops, a custom LabView program was used to control the electronics. The program was setup to run an individual hysteresis loop and then store the data in

a single file. A single measurement does not give enough resolution to make an accurate assessment of the hysteresis loop. To collect high-resolution data (i.e., good statistics), one can measure several loops for a given angle and sum over the intensity, which will yield a smooth hysteresis loop that can be normalized without losing the detailed features of the loop. Once all of the features have been resolved for several angular orientations of the sample with respect to the plane of incidence, the data can be compared. Figure 3.3 shows four the hysteresis loops taken for Co_2MnAl

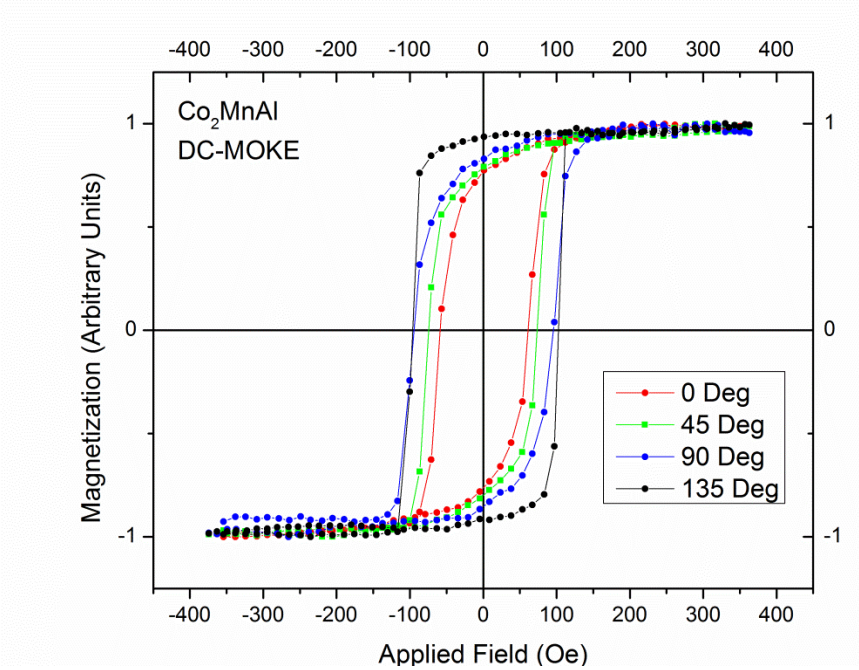

Figure 3.3. Normalized hysteresis loops of Co_2MnAl for the angles of 0˚, 45˚, 90˚, 135˚ orientation.

In theory, since the DC curves are a direct result of the Kerr effect, one should be able to get a rough estimate of the Kerr rotation using the DC curve. Using Malus' law,

$$I=I_0\cos^2\theta, \tag{3.1}$$

which can be used to calculate the angle between two polarizers, one can estimate the DC Kerr effect. However, instead of calculating the angle between two polarizers, the angle between the polarizer and the final polarization at the detector (θ) is calculated. I_0 is the maximum intensity for a given θ. By carefully measuring I_0 and the angle through which the analyzer has been rotated, the angle of polarization at the maximum and minimum saturation magnetization can be determined by directly applying Malus' law. The difference between the angles should give a value close to twice that of the Kerr rotation. This measurement however is just a rough estimate. It was found to be highly dependent upon the angle of the analyzer. For example, when the analyzer was rotated 2.0° off the minimum the calculated Kerr rotation was 0.020 degrees for Co_2MnAl, compared to when it was only rotated 1.0° it was found to be 0.025 degrees, an increase in 25 %.

For each target, the total Kerr rotation was measured using Malus' law. The analyzer was rotated two degrees away from extinction. The rotator used has an uncertainty of approximately 0.1 degrees. Although the nanovoltmeter used to measure the intensity can accurately measure the voltage, the signal was only stable to the third significant digit. When measuring I_0, the uncertainty was 0.01V, but when measuring the intensity near extinction the uncertainty was reduced to 0.01mV. In each case the fractional uncertainty is approximately one percent. One can determine the standard deviation for each point in the plot and determine the fractional uncertainty. Averaging those together gives an average uncertainty of 0.06%. Although the fractional uncertainty (regarding the inherent uncertainty of the electronics) is so small, the actual uncertainty is much larger due to the optical setup as discussed above.

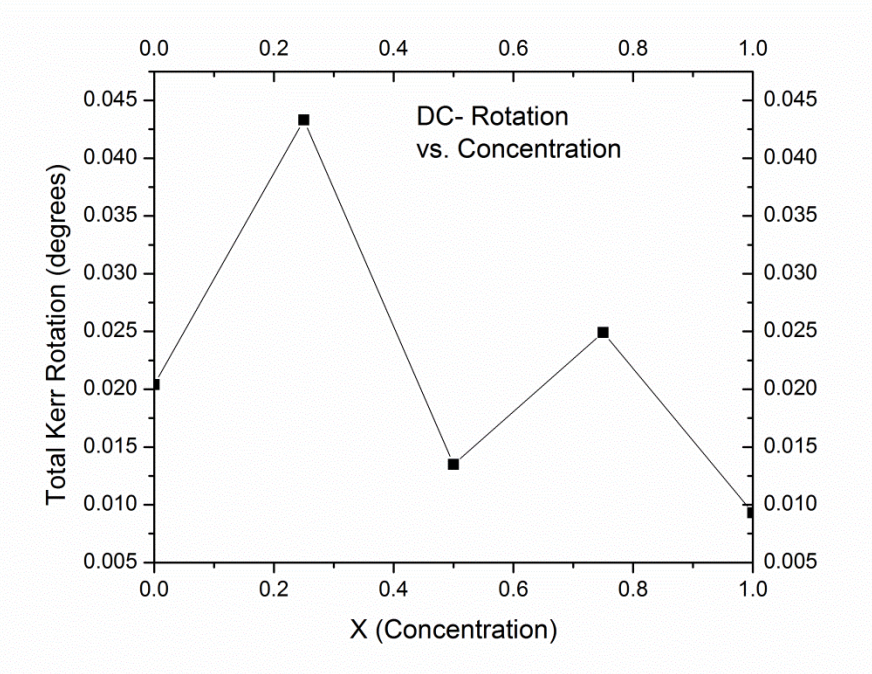

Figure 3.4. The DC-Rotation measurements taken using Malus' law do not show a consistent trend along the series.

3.2 AC-MOKE

Although information about the coercive field and saturation field can be obtained, the main objective of this thesis is to understand the AC Kerr effect in the samples. The DC-MOKE measurements can be taken quickly and thus can be used to help determine the angle and settings to be used in the AC-MOKE measurements. The Kerr rotation is the change in angle from the origin to the saturation. The best measurements of the saturation magnetization are done near the easy axis. The DC-MOKE is a result of the total Kerr rotation and thus the AC measurements should follow the same shape as the DC curves.

The AC-MOKE setup and measurements were the main focus of this thesis. For each film the Kerr rotation and Kerr ellipticity were carefully measured using the optical setups as

described in previous sections. After determining the best angle at which to take the AC-MOKE measurements using the DC-MOKE measurements, the Kerr rotation was measured after placing the PEM at zero degrees between the sample and the analyzer. The analyzer was rotated to 45 degrees. Again the computer only measures individual runs and records the applied field, the DC intensity, the AC intensity of the second harmonic, and the Kerr rotation at each point. The computer uses Equation 2.17 to calculate the Kerr rotation at each point. The individual runs have a high degree of uncertainty and the signal has a large amount of background noise, but by averaging over several runs, one can make a clean plot of Kerr rotation versus applied field. The difference between the upper and lower saturation is twice the Kerr angle. The measurements were then normalized so that the hysteresis loops were symmetric about zero (See Figure 3.5 B).

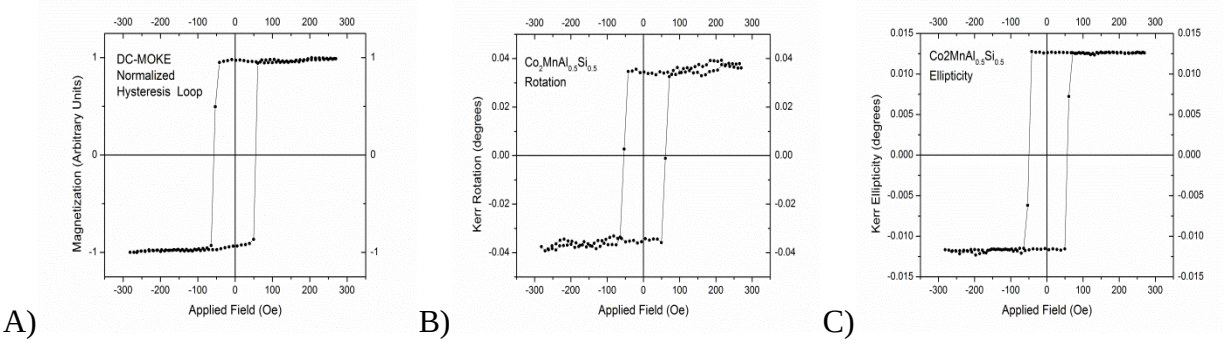

Figure 3.5. A) The normalized DC-MOKE setup of $Co_2MnAl_{0.5}Si_{0.5}$ B) The normalized Kerr rotation a for $Co_2MnSi_{0.5}Al_{0.5}$ C) The normalized ellipticity for $Co_2MnAl_{0.5}Si_{0.5}$

The Kerr ellipticity was the final measurement. The PEM was rotated to 45˚and the analyzer was rotated to 90˚. This optical setup gives a very low signal to noise ratio [39]. The AC intensity of the first harmonic was the first measured for the ellipticity. The LabView program is setup to take this into account when calculating the Kerr ellipticity. Similar to measuring the Kerr rotation, several individual runs were taken and averaged to produce a clean plot (Figure

3.5 C). The Kerr ellipticity is twice the difference between the values at the upper and lower saturation.

Both the rotation and ellipticity were measured for each film to confirm the measurements. The measurements for the DC-rotation, the AC-rotation, and the AC-ellipticity are recorded in Table 3.1. Figure 3.6 A shows plot of Kerr rotation versus x. The value ranges from 0.028 degrees for pure Si to 0.034 degrees for pure Al. The uncertainty in the values are approximately 0.001. Although the uncertainty in the voltage measurements is near 0.5 %, the uncertainty in the value of K_2 is much larger, near 3%, significantly increasing the uncertainty in the calculation of the Kerr rotation. The x=0.50 sample has the same rotation as the Co_2MnAl. Additional runs of the $Co_2MnAl_{0.5}Si_{0.5}$ were able to confirm the higher value of the rotation.

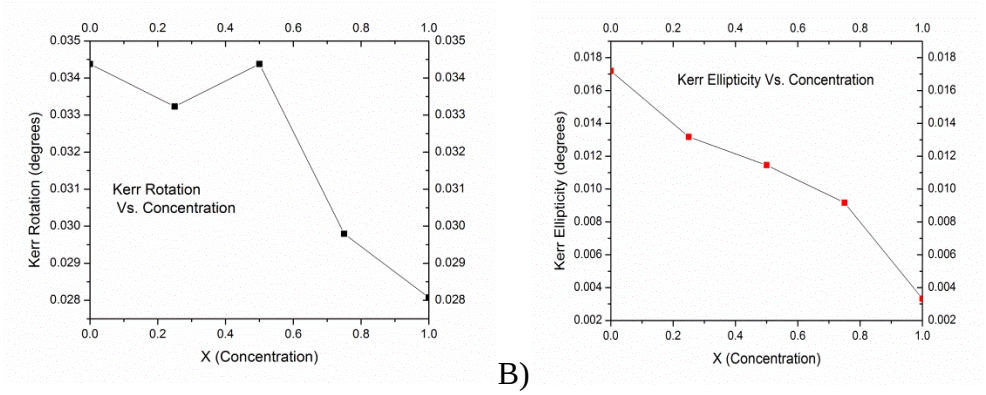

A) B)

Figure 3.6. A) The Kerr rotation versus X concentration for $Co_2MnSi_xAl_{1-x}$ B) The Kerr ellipticity versus X concentration for $Co_2MnSi_xAl_{1-x}$

The values of the Kerr ellipticity are plotted in Figure 3.6 B. The Kerr ellipticity increases with percentage Al starting at 0.003 degrees for pure Si to 0.017 degrees. The sources of uncertainty in the Kerr ellipticity are the same sources as the Kerr rotation. The fractional

uncertainty of the Kerr ellipticity is also approximately 3%, since the value of K_2 is again the dominate source of uncertainty.

The uncertainties for these measurements are all conservative estimates since the experiment has several sources of error. The sources in error in the DC Malus' law measurements are due to the significant change in the value of the rotation based on the angle of the analyzer as discussed above. As for the AC-Kerr rotation and Kerr ellipticity, the uncertainty in the individual measurements can be largely due to the background noise in the AC-intensity. This is reduced when calculating the standard deviation for the measurement. The background noise is increased due to the angle of the PEM and the analyzer. The uncertainty in the angle of the rotator used for the analyzer is 0.1°. Due to the placement of the analyzer at the center of the optical table, the micrometer can be difficult to read increasing the uncertainty to approximately 0.2°. This angle of the analyzer changes affects the measured value of the intensity. The larger source of uncertainty in the AC measurements comes from the angle of the PEM. The transmission axis of the PEM used is not directly along the axis of the casing of the optics. To compensate for off axis PEM, a homemade mount was used to attach the PEM to a rotator. This gave the advantage of easily being able to move between the optical configurations for the rotation and ellipticity measurements at the cost greater uncertainty in the angle of the transmission axis of the PEM. The angle of the PEM is important due to the fact that fine adjustments of the PEM make significant changes in the magnitude and oscillation of the measured peaks (first and second harmonic peaks).

Table 3.1 The values of DC-Rotation, Kerr rotation, and Kerr ellipticity calculated for each target material.

	Co_2MnAl	$Co2MnSi_{0.25}Al_{0.75}$	$Co2MnSi_{0.5}Al_{0.5}$	$Co2MnSi_{0.75}Al_{0.25}$	Co_2MnSi
DC-Rotation	0.020	0.043	0.014	0.025	0.009
Kerr Rotation	0.034	0.033	0.034	0.030	0.028
Kerr Ellipticity	0.017	0.013	0.012	0.009	0.003

3.3 Discussion and Conclusions

The purpose of this thesis was to design and assemble a working AC-MOKE measurement system and to acquire initial measurements of Kerr rotation and Kerr ellipticity of Heulser alloy thin films. Although the measurements were taken to a reasonable degree of uncertainty, a comparison and calibration is needed. There have not been any measurements of the Kerr rotation or ellipticity for the $Co_2MnSi_xAl_{1-x}$ series, but theoretical calculations and experimental measurements have been done on similar Heusler alloys [28, 40, 46].

The Kerr rotation and ellipticity are dependent upon the photon energy of the light source and the initial polarization [40]. The photon energy of the 640 nm laser used 1.94 eV. The polarizer was rotated to produce s-wave polarization. Ricco et al. calculated the theoretical Kerr rotation and Kerr ellipticity for Co_2MnGe and Co_2MnSn for both s- and p- polarized light in this study. The Kerr rotation near 1.9 eV for s-polarized light for both samples was approximately 0.020 degrees. The value of the Kerr ellipticity at the same photon energy and polarization was about 0.002 degrees for Co_2MnSn and 0.008 for Co_2MnGe.

The measured values for the rotation of the $Co_2MnSi_xAl_{1-x}$ are roughly 50% larger than the comparison values calculated and measured by Ricco et al [40]. Hamrle et al. measured the

Kerr rotation for Co_2FeSi. In this study, the longitudinal Kerr rotation was reported to be 0.010 degree, approximately one third of our measured rotations of the Co_2MnSi, but was near the DC-MOKE measured value (0.009deg) [28]. The range of values for the Kerr ellipticity calculated and measured by Ricco et al show a large range of values. The $Co_2MnAl_xSi_{1-x}$ Kerr ellipticity is within the range of the values of the Co_2MnGe and Co_2MnSn Kerr ellipticity. Although there are no direct comparisons for $Co_2MnAl_xSi_{1-x}$ the measured Kerr rotation and ellipticity are intuitively valid measurements based on the comparison to other Heusler alloys.

Although the longitudinal AC-MOKE measurements taken for this thesis compare well with theoretical and experimental values of similar Heusler alloys, the measurements can be significantly improved by calibrating the system with standards. The next step in setting up the AC-system is to fabricate a film of a material with a well-known Kerr rotation and ellipticity, such as pure Co, Ni, or Fe.

References

[1] M. Faraday, *Experimental Researches in Electricity, Nineteenth Series*, Philosophical Transactions of the Royal Society (London) 5, (1846) 592.

[2] J. Kerr, *On Reflection of Polarized Light from the Equatorial Surface of a Magnet*, Philosohical Magazine 5, 167 (1878).

[3] P. Argyres, *Theory of the Faraday and Kerr Effects in Ferromagnetics*, Physics Review 99, 334 (1955).

[4] Z. Qiu and S. Bader, *Surface Magnetism and Kerr Spectroscopy*, MRS Bulletin 20, 10 (1995) 34.

[5] E.Moog and S. Bader, *Smoke signals from ferromagnetic monolayers: p(1×1) Fe/Au(100),* J. Superlattices Microstructure 1, 543 (1985).

[6] S. Bader, C. Liu, *Issues in Surface Magnetism*, Journal of Vacuum Science and Technologies A 9, 1924 (1991).

[7] S. Bader, *SMOKE*, Journal of Magnetism and Magnetic Materials 100, 440 (1991).

[8] Z. Qui and S. Bader, *Surface Magneto-optic Kerr Effect*, Journal of Magnetism and Magnetic Materials 200, 664 (1999).

[9] R. Kawakami, doctoral dissertation, UC Berkeley (1999).

[10] Zak J., Moog E.R., Liu C., Bader S.D., *Fundamental magneto-optics*, Journal of Applied Physics 68, 4203 (1990).

[11] Zak J., Moog E.R., Liu C., Bader S.D., *Universal approach to magneto-optics*, Journal of Magnetism and Magnetic Matererial 89, 107 (1990).

[12] You C., Shin S., *Simplified analytic forulae for magneto-optical Kerr effects in ultrathin magnetic films*, Journal Magnetism and Magnetic Materials, 198, 573 (1994).

[13] T Oakberg, Hinds Application Note, *Magneto-Optic Kerr Effect*, June 4, 2012, http://www.hindsinstruments.com/wp-content/uploads/MOKE.pdf.

[14] D. Chrisey, G. Hubler, Pulsed Laser Deposition of Thin Films, (188),(192), John Wiley and Sons, inc, New York, 1994.

[15] H. Smith, A.F. Turner, Vacuum Deposited Thin Films Using a Ruby Laser, Applied Optics, 4 ,1 , 147 (1965).

[16] D. Dijkkamp, et al., *Process for Making Thin Polymer Film bt Pulsed Laser Evaporation*, Applied Physics Letters 51, 619 (1987).

[17] A. Beavitt, *A wide-band particle eliminator*, Thin Solid Films 1, 69 (1967).

[18] R. J. Kennedy, *A new laser ablation geometry for the production of smooth thin single-layer $YBa_2Cu_3O_{7-x}$ and multilayer $YBa_2Cu_3O_{7-x}/PrBa_2Cu_3O_{7-x}$ films*, Thin Solid Films, 214 (2), 223 (1992).

[19] D. S. Misra, S. B. Palmer, *Laser ablated thin films of Y, Ba_2Cu_3 0_0: the nature and origin of the particulates*. Physica C: Superconductivity, *176* (1), 43 (1991).

[20] G.A. Prinz, *Device Physics: Magnetoelectronics*, Science 282, 1660 (1999).

[21] G.A. Prinz, *Spin Polarized Transport*, Physics Today 48, 58 (1995).

[22] G.A. Prinz, K. Hathaway, *Special Issue: Magnetoelectronics*, Physics Today 48, 24 (1995).

[23] W. A. Picket, J.A. Moodera, *Half Metallic Magnets*, Physics Today 54 (5), 39 (2001).

[24] S. Bludel, *Magnetism in Condensed Matter*, New York, Oxford University Press, (2001).

[25] F. Heusler, *Über magnetische Manganlegierungen* (in German). Verhandlungen der Deutschen Physikalischen Gesellschaft **5**: 219. (1903).

[26] M.A. Ruderman ,C. Kittel, *Indirect Exchange Coupling of Nuclear Magnetic Moments by Conduction Electrons*, Physics Review 96, 99 (1954).

[27] DeGroot R A, Mueller FM, van Engen PG, Buschow K H J, *New Class of Materials: Half-Metallic Ferromagnets*, Physics Review Letters 50, 2024 (1983).

[28] Hamrle, J., Blomeier, S., Gaier, O., Hillebrands, B., Schneider, H., Jakob, G. and Felser, C., *Huge quadratic magneto-optical Kerr effect and magnetization reversal in the Co_2FeSi Heusler compound*, Journal of Physics D: Applied Physics 40, 1563 (2007) .

[29] Kubota, T., Hamrle, J., Gaier, O., and Hillebrands, B. 6.8 *$Co_2MnAl_xSi_{1-x}$ Heusler compound investigated by Brillouin light spectroscopy and magneto-optical Kerr effect magnetometry.* AG Manetismus Annual Report, 53 (2007).

[30] I. Galanakis, K. Ozdogan, E.Sasioglu, and B. Aktas, *Defects in CrAs and related compounds as a route to half-metallic ferrimagnetism*, Physical Review B Rapid Communications 74, 140408(R) (2006).

[31]Wang W. H., Przybylski M., Kuch W., Chelaru L. I., Wang J., Lu Y. F.,Barthel J., Meyerhei m H. L., Kirschner, J.*Magnetic properties and spin polarization of Co_2MnSi Heusler alloy thin films epitaxially grown on GaAs (001)*,Physical Review B **71**, 144416 (2005).

[32] Ritchie, Lance, Gang Xiao, Y. Ji, T. Y. Chen, C. L. Chien, Ming Zhang, Jinglan Chen, Zhuhong Liu, Guangheng Wu, and X. X. Zhang, . *Magnetic, structural, and transport properties of the Heusler alloys Co_2MnSi and NiMnSb,* Physical Review B **68**, 104430 (2003).

[33] N. Shigekazu, *Spin polarization of field-emitted electrons from half-metallic Co2MnSi thin films grown on a W(001)facet*, Ultramicroscopy 109, 396 (2009).

[34] C. Grigorescu et al., *Co_2MnX (X=Si,Ge , Sn, Sb, Sn) thin films grown by pulsed-laser deposition*, Journal of Crystal Growth 275, 1183 (2005).

[35] H. Schneider, E. Vilanova, B. Balke, C. Felser, and G. Jakob ,*Hall effect in laser ablated $Co_2(Mn,Fe)Si$ thin films,* Journal of Physics D: Applied Physics **42,** 84012 (2009).

[36] Y. J. Chen, D. Basiaga, J. R. O'Brien, D. Heiman, *Anomalous magnetic properties and Hall effect in ferromagnetic Co2MnAl epilayers,* Applied Physics Letters 84, 4301 (2004).

[37] M. Obaida, K. Westerholt, H. Zabel, *Magnetotransport properties of Cu_2MnAl, Co_2MnGe, and Co_2MnSi Heusler alloy thin films: From nanocrystalline disordered state to long-range-ordered crystalline state*, Physical Review B **84**, 184416 (2011).

[38] M. P. Raphael, B. Ravel, M. A. Willard, S. F. Cheng, B. N. Das, Stroud, R. M., Bussmann, K. M., Claassen, J. H., and Harris, V. G., *Magnetic, structural, and transport properties of thin film and single crystal Co_2MnSi*, Applied Physics Letters **79**, 4396 (2001).

[39] I.Galanikis, P.H. Dederichs, *Slater-Pauling behavior and origin of the half-metallicity of the full-Heusler alloys*, Physics Review B. 66, 174429 (2002).

[40] Fabio Ricci, Silvia Picozzi, Alessandra Continenza, Franco D'Orazio, Franco Lucari, Kurt Westerholt, Miyoung Kim,Arthur J. Freeman., *Optical and magneto-optical properties of ferromagnetic full-Heusler films: Experiments and first-principles calculations*, Physics Review B, 76, 014425 (2007).

[41] Galanakis, I., Şaşıoğlu, E., Özdoğan, K., *Magnetic phase transition in half-metallic CoMnSb and NiMnSb semi-Heusler alloys upon Cu doping: First-principles calculations,* Physics Review B 77, 21, 214417 (2008).

[42] Paudel M., Wolfe C., Patton H., Dubenko I., Ali, N., Christodoulides J.A., Stadler S., *Magnetic and Transport Properties of $Co_2MnSn_xSb_{1-x}$ Heusler Alloys*, Journal of Applied Physics 1, 105 (2009).

[43] D. Kliger, J. Lewis, C. Randall, *Polarized Light in Optics and Spectroscopy*, Boston: Academic Press Inc., (1990).

[44] R. Atkinson, 2001, *Magnetism in a New Light*, Hinds News Letter, Fall 2001.

[45] *Detecting the Ratio of I_{AC}/I*, Hinds Application Note, July, 17, 2012, http://www.hindsinstruments.com/wp-content/uploads/Determining_Ratio.pdf.

[46] Polisetty, S., Scheffler, J., Sahoo, S., Wang, Y., Mukherjee, T., He, X., and Binek, C., *Optimization of magneto-optic Kerr setup: Analyzing experimental assemblies using Jones matrix formalism*, Review of Scientific Instruments **79,** 055107 (2008).

[47] Winter A. , Pascher H., Krenn H., Wojtowicz T., Liu X., and Furdyna J. K., *Kerr Rotation and Magnetic Circular Dichroism Spectra of Ferromagnetic InMnSb and InMnAs*, Review Advanced Material Science 20, 92 (2009).

Appendix A
Determination of the Fresnel Coefficients

To derive the Fresnel coefficients, it is necessary to define the matrices $\boldsymbol{F}$ and $\boldsymbol{P}$ as

$$\boldsymbol{F} = \begin{pmatrix} E_x \\ E_y \\ H_x \\ H_y \end{pmatrix} \tag{A.1}$$

$$\boldsymbol{P} = \begin{pmatrix} {E_s}^{(i)} \\ {E_p}^{(i)} \\ {E_s}^{(r)} \\ {E_p}^{(r)} \end{pmatrix}, \tag{A.2}$$

which are related by the relation

$$\boldsymbol{F} = A\boldsymbol{P}. \tag{A.3}$$

$\boldsymbol{F}$ is the boundary-field matrix, which describe the electric and magnetic field at the boundary between two media. The $\boldsymbol{P}$-matrix describes the electric field of incident and reflected wave in terms of the s- and p-polarized light. A is the medium boundary matrix relating $\boldsymbol{F}$ and $\boldsymbol{P}$. The advantage of using the $\boldsymbol{P}$ matrix is it allows boundary conditions to be written in terms of the magneto-optic constant, Q.

The medium boundary matrix, A_j (derived fully in Ref. [40]), for a the boundary of the j^{th} layer with an arbitrary magnetization is given by

$$A_j = \begin{pmatrix} 1 & 0 & 1 & 0 \\ \frac{iQ{\alpha_{yj}}^2}{2}\left(m_y\frac{1+{\alpha_{zj}}^2}{\alpha_{yj}\alpha_{zj}} - m_z\right) & \alpha_{zj} & \frac{-iQ{\alpha_{yj}}^2}{2}\left(m_y\frac{1+{\alpha_{zj}}^2}{\alpha_{yj}\alpha_{zj}} + m_z\right) & -\alpha_{zj} \\ \frac{-in_jQ}{2}\left(m_y\alpha_{yj} + m_z\alpha_{zj}\right) & -n_j & \frac{-in_jQ}{2}\left(m_y\alpha_{yj} + m_z\alpha_{zj}\right) & -n_j \\ n_j\alpha_{zj} & \frac{-in_jQ}{2}\left(m_y\frac{\alpha_{yj}}{\alpha_{zj}} - m_z\right) & -n_j\alpha_{zj} & \frac{in_jQ}{2}\left(m_y\frac{\alpha_{yj}}{\alpha_{zj}} + m_z\right) \end{pmatrix} \tag{A.4}$$

where $\alpha_{yj} = \sin\theta_j$ and $\alpha_{zj} = \cos\theta_j$[10, 11, 12]. Also, the m_j are the directional cosines of the magnetization vector **M** as shown in the Figure A.1 with the angles defined in Figure A.2:

$$m_x = \sin\varphi\cos\gamma$$

$$m_y = \sin\varphi\sin\gamma \tag{A.5}$$

$$m_z = \cos\varphi$$

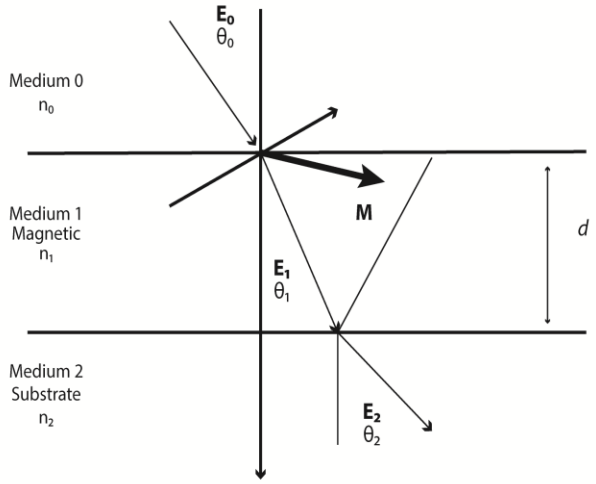

Figure A.1 Side view of a single layer film magnetic film with magnetization **M**. Medium 0 is the ambient atmosphere. The incoming electric field will be bent as it enters the next medium according to Snell's law.

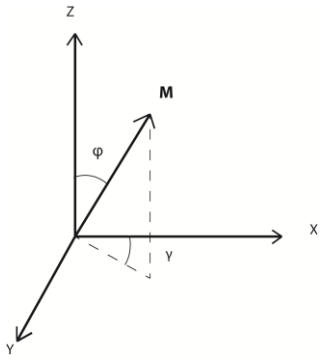

Figure A.2 The angle φ is defined as the angle between the magnetization vector and the z-axis while γ is the angle between the projection of the magnetization vector onto the xy-plane and the x axis.

The medium boundary matrix can be used to determine $\boldsymbol{P_j}$, where $\boldsymbol{P_j}$ is the $\boldsymbol{P}$ matrix for the j^{th} layer, by using the relation

$$A_j \boldsymbol{P_j} = A_{j+1} \boldsymbol{P}_{j+1}. \tag{A.6}$$

For the case of s-polarized light (i.e., ${E_{(j+1)p}}^{(r)} = {E_{(j+1)p}}^{(r)}\, {E_{jp}}^{(i)} = 0$), the Fresnel coefficients are defined by

$$r_{ss} = \frac{{E_{js}}^{(r)}}{{E_{js}}^{(i)}}, \qquad r_{ps} = \frac{{E_{jp}}^{(r)}}{{E_{js}}^{(i)}}, \qquad t_{ss} = \frac{{E_{(j+1)s}}^{(i)}}{{E_{js}}^{(i)}}, \qquad t_{ps} = \frac{{E_{(j+1)p}}^{(i)}}{{E_{js}}^{(i)}}, \tag{A.7}$$

where t_{ss} and t_{ps} is the Fresnel transmission coefficients. For the case of s-polarized light, one can divided both sides Equation (A.6) by ${E_{js}}^{(i)}$, yielding

$$A_j \begin{pmatrix} 1 \\ 0 \\ r_{ss} \\ r_{ps} \end{pmatrix} = A_{j+1} \begin{pmatrix} t_{ss} \\ t_{ps} \\ 0 \\ 0 \end{pmatrix}, \tag{A.8}$$

which describes the interaction at the intersection of two media.

As the light passes through the medium, it will interact with the material. The interaction with the material can be represented by a medium propagation matrix that describes the interaction of the electric field with the material. It is important to note that this can be used to describe both magnetic and non-magnetic media depending on the value of *Q*. For a generally polarized beam (a mixture of both s- and p- light), the incoming beam will be split into two separate beams due to the birefringence of the material, each of which will have an incident and reflected component in the medium. The matrix *D* describes the relationship between the four electric fields at each of the boundaries of the film. One can then define a matrix ***S*** that describes the relationship between the *x* component of the electric fields of the four beams and the ***P*** matrix [11]. The matrix ***S*** can then be used to perform a coordinate transformation on *D*, resulting in a matrix that defines the propagation of the light through the medium in terms of ***P*** matrix. This is desired, since the matrix *A* is defined in terms of the ***P***. The medium propagation matrix is derived fully in Ref [11] and is given by

$$\overline{D} = \begin{pmatrix} U\cos\delta^i & U\sin\delta^i & 0 & 0 \\ -U\sin\delta^i & U\cos\delta^i & 0 & 0 \\ 0 & 0 & U^{-1}\cos\delta^r & -U^{-1}\sin\delta^i \\ 0 & 0 & U^{-1}\sin\delta^i & U^{-1}\cos\delta^r \end{pmatrix}, \tag{A.9}$$

where *U* represents the exponential decay of the beam as it passes through the magnetic medium and is given by

$$U = exp\left(-i\frac{2\pi}{\lambda}n_j\alpha_{zj}d\right). \tag{A.10}$$

The angle $\delta^{i,r}$ is defined by

$$\delta^{i,r} = -\frac{\pi n_j Q d_j g^{i,r}}{\lambda \alpha_{zj}} \tag{A.11}$$

and $g^{i,r}$ is

$$g^{i,r} = m_z \alpha_{zj} \pm m_y \alpha_{yj}. \tag{A.12}$$

Now that both A and $\overline{D}$ are defined, they can be used to describe interaction of light with a single layer film of thickness d. In this case there are three interactions that must be taken into account: the boundary at the surface of the film, the boundary between the film and the substrate, and the propagation through the film. Applying Equation (A.6) yields

$$A_0 \boldsymbol{P}_0 = A_1 \boldsymbol{P}_1(0) = A_1 \overline{D} \boldsymbol{P}_1(d) = A_1 \overline{D} {A_1}^{-1} A_1 \boldsymbol{P}_1(d) = A_1 \overline{D} {A_1}^{-1} A_2 \boldsymbol{P}_2(d)\,, \tag{A.13}$$

where $\boldsymbol{P}_1(0)$ represents the $\boldsymbol{P}$ matrix of the film at the surface, and $\boldsymbol{P}_1(d)$ represents the $\boldsymbol{P}$ matrix of the film at the substrate. Equation (A.13) represents a general case in which any of the three media can be either magnetic or non-magnetic. The most common case though is when medium 1 and 3 are non-magnetic and medium 2 is magnetic. By applying Equation (A.7) for s-polarized incident waves, this will yield

$$A_0 \begin{pmatrix} 0 \\ 1 \\ r_{ss} \\ r_{ps} \end{pmatrix} = A_1 \overline{D} {A_1}^{-1} A_2 \begin{pmatrix} t_{ss} \\ t_{ps} \\ 0 \\ 0 \end{pmatrix} \tag{A.14}$$

And for p- polarization

$$A_0 \begin{pmatrix} 0 \\ 1 \\ r_{sp} \\ r_{pp} \end{pmatrix} = A_1 \overline{D} {A_1}^{-1} A_2 \begin{pmatrix} t_{sp} \\ t_{pp} \\ 0 \\ 0 \end{pmatrix} \tag{A.15}$$

To solve for the Fresnel coefficients, Equation (A.14) is used to determine a 4x4 matrix given by the expression,

$$M = {A_0}^{-1} A_1 D_1 {A_1}^{-1} A_2, \tag{A.16}$$

which be expressed as to the 2 x 2 matrix.

$$M = \begin{pmatrix} G & H \\ I & J \end{pmatrix}, \tag{A.17}$$

where *G*, *H*, *I*, and *J* are 2x 2 block matrices.

For the general case of either s- or p- polarization, one can define a two component column vector for the incident beam and the reflected beam:

$${E_0}^{(i,r)} = \begin{pmatrix} {E_{0s}}^{(i,r)} \\ {E_{0p}}^{(i,r)} \end{pmatrix}, \tag{A.18}$$

where *i* and *r* represent the incident and reflected beams, respectively. Then, by using Equation (A.14) and (A.15) (before applying equation 7), it can be shown that

$${E_0}^{(r)} = IG^{-1}{E_0}^{(i)}, \tag{A.19}$$

which directly yields

$$\begin{pmatrix} r_{ss} & r_{sp} \\ r_{ps} & r_{pp} \end{pmatrix} = IG^{-1}, \tag{A.20}$$

where *G* and *I* are given by

$$G = \begin{pmatrix} \frac{1}{2} + \frac{n_2 \cos\theta_2}{2n_0 \cos\theta_0} - \frac{id_1\pi(n_0 n_2 \cos\theta_0 \cos\theta_2 + {n_1}^2 cos^2\,\theta_1)}{\lambda n_0 \cos\theta_0} & -\frac{n_1 d_1 \pi Q(m_z n_1 \cos\theta_2 + m_y n_2 \sin\theta_1)}{\lambda n_0 \cos\theta_0} \\ \frac{n_1 d_1 \pi Q(m_z n_1 \cos\theta_0 + m_y n_0 \sin\theta_1)}{\lambda n_0 \cos\theta_0} & \frac{n_2}{2n_0} + \frac{\cos\theta_2}{2\cos\theta_0} - \frac{id_1\pi(n_0 n_2\, cos^2\,\theta_1 + {n_1}^2 \cos\theta_0 \cos\theta_2)}{\lambda n_0 \cos\theta_0} \end{pmatrix} \tag{A.21}$$

$$I = \begin{pmatrix} \frac{1}{2} - \frac{n_2 \cos\theta_2}{2n_0 \cos\theta_0} - \frac{id_1\pi\left(n_0 n_2 \cos\theta_0 \cos\theta_2 - {n_1}^2 cos^2\,\theta_1\right)}{\lambda n_0 \cos\theta_0} & -\frac{n_1 d_1 \pi Q\left(m_z n_1 \cos\theta_2 + m_y n_2 \sin\theta_1\right)}{\lambda n_0 \cos\theta_0} \\ \frac{n_1 d_1 \pi Q\left(m_z n_1 \cos\theta_0 - m_y n_0 \sin\theta_1\right)}{\lambda n_0 \cos\theta_0} & \frac{n_2}{2n_0} - \frac{\cos\theta_2}{2\cos\theta_0} + \frac{id_1\pi\left(n_0 n_2\, cos^2\,\theta_1 + {n_1}^2 \cos\theta_0 \cos\theta_2\right)}{\lambda n_0 \cos\theta_0} \end{pmatrix}. \quad \text{(A.22)}$$

Although the results above have been shown for a single layer film, the above method can be used for a film of any number of layers by determining the matrix *M*. Equation (A.22) is still valid for multilayer films [11].

Appendix B
List of Components for MOKE Measurements

Coherent

1 OBIS 640 nm diode laser with heat sink and control box

Thor Labs

2 PRM1 High Precision Rotation Mount

2 SM1PM10 Lens Tube Mount

2 GT10-A 10mm Glan-Taylor Polarizer

New Focus

2 9731 Optical Rail, 3.0 in Width, 12 in. length

6 9739 Optical Rail Table Clamp

4 9741 1 in. Optical Rail Carrier

1 9026 Riser Carrier

1 9742 2 in Optical Rail Carrier

8 8-32 Post

1 ¼-20 Post

5 3 in. Post Holders

3 9641 Open Cage L-Element Carrier

3 9642 Open Cage U-element Carrier

4 10 in. Stainless Steel Rods (1/4 in. diameter)

2 4 in. Stainless Steel Rods (1/4 in. diameter)

Newport

1 460A Quick-mount linear stage

Melles Griot

1 360˚Prism rotator

Hinds

1 DET-100-002 Photodetector

1 SCU-100 Signal Conditioner

1 PEM-90 Photoelastic Modulator with PEM Head

Miscellaneous

1 Tektronic TDS 2012 Oscilloscope

1 Keithley 2182 Nanovoltmeter

1 Stanford Research systems SR 850 DSP Lock-In Amplifier

1 Lakeshore 421 Gaussmeter with probe

2 Kepco Bipolar Operational Power Supply/ Amplifier

3 GPIB cables

2 Coaxial cable to Banana Clip connectors

2 Coaxial cable to Alligator Clip connectors (with shielding)

2 Coaxial cable splitters

1 Custom PEM Rotator Mount

1 Custom Magnet with custom mount

1 Custom Rotating sample mount

1 36 in. by 36 in. optical table

Vita

Matthew Champagne grew up the youngest of six children in the small city of Houma, near the Gulf coast of Louisiana. In 2006 he graduated summa cum laude from Vandebilt Catholic High School. He continued his education the next semester at Louisiana State University (LSU) after being accepted into the Louisiana science, technology, engineering, and mathematics (LA-STEM) program. He began his research career under Dr. David Young and Dr. Phillip Adams at the same time he began classes. Four years later, in 2010, Matthew graduated with his BSc in physics. He was again accepted to LSU, only this time as a graduate student in physics. After taking a year off from research, he began working under Dr. Phillip Sprunger, learning about both vacuum and surface science. The next summer (2012) he began his thesis project under Dr. Shane Stadler. After successfully defending his thesis in December of the same year, he will receive his master degree with a concentration in condensed matter physics in May of 2013.